

# Hard X-Ray Properties of the Merging Cluster Abell 3667 as Observed with Suzaku

Kazuhiro NAKAZAWA

*Department of Physics, The University of Tokyo, 7-3-1 Hongo, Bunkyo-ku, Tokyo 113-0033  
nakazawa@amalthea.phys.s.u-tokyo.jp*

Craig L. SARAZIN

*Department of Astronomy, University of Virginia, P.O. Box 400325, Charlottesville, VA 22904-4325, USA*

Madoka KAWAHARADA

*Cosmic Radiation Laboratory, RIKEN, 2-1 Hirosawa, Wako, Saitama 350-0198*

Takao KITAGUCHI and Sho OKUYAMA

*Department of Physics, The University of Tokyo, 7-3-1 Hongo, Bunkyo-ku, Tokyo 113-0033*

Kazuo MAKISHIMA

*Department of Physics, The University of Tokyo, 7-3-1 Hongo, Bunkyo-ku, Tokyo 113-0033*

*Cosmic Radiation Laboratory, RIKEN, 2-1 Hirosawa, Wako, Saitama 350-0198*

Naomi KAWANO and Yasushi FUKAZAWA

*Department of Physical Science, Hiroshima University, 1-3-1 Kagamiyama, Higashi-Hiroshima, Hiroshima 739-8526*

Susumu INOUE

*Department of Physics, Kyoto University, Oiwake-cho, Kitashirakawa, Sakyo-ku, Kyoto 606-8502*

Motokazu TAKIZAWA

*Department of Physics, Yamagata University, 1-4-12 Kojirakawa-machi, Yamagata, Yamagata 990-8560*

Daniel R. WIK

*Department of Astronomy, University of Virginia, P.O. Box 400325, Charlottesville, VA 22904-4325, USA*

Alexis FINOGENOV

*Max-Planck-Institut für extraterrestrische Physik, Giessenbachstraße, 85748 Garching, Germany*

*University of Maryland, Baltimore County, 1000 Hilltop Circle, Baltimore, MD 21250, USA*

and

Tracy E. CLARKE

*Naval Research Laboratory, 4555 Overlook Ave. SW, Code 7213, Washington D.C. 20375*

*Interferometrics Inc., 13454 Sunrise Valley Drive, Suite 240, Herndon, VA 20171, USA*

(Received 2008 August 6; accepted 2008 December 4)

## Abstract

Wide-band Suzaku data on the merging cluster Abell 3667 were examined for hard X-ray emission in excess to the known thermal component. Suzaku detected X-ray signals in a wide energy band from 0.5 to 40 keV. The hard X-ray ( $> 10$  keV) flux observed by the HXD around the cluster center cannot be explained by a simple extension of the thermal emission with an average temperature of  $\sim 7$  keV. The emission is most likely to be from a very hot ( $kT > 13.2$  keV) thermal component around the cluster center, produced via a strong heating process in a merger. In the north-west radio relic, no signature of non-thermal emission was observed. Using the HXD, the overall upper-limit flux within a  $34' \times 34'$  field-of-view around the relic was derived to be  $5.3 \times 10^{-12}$  erg  $s^{-1}$   $cm^{-2}$  in the 10–40 keV band, after subtracting the ICM contribution estimated using the XIS or the XMM-Newton spectra. Directly on the relic region, the upper limit is further tightened by the XIS data to be less than  $7.3 \times 10^{-13}$  erg  $s^{-1}$   $cm^{-2}$ , when converted into the 10–40 keV band. The latter value suggest that the average magnetic field within the relic is higher than  $1.6 \mu\text{G}$ . The non-thermal pressure due to magnetic fields and relativistic electrons may be as large as  $\sim 20\%$  of the thermal pressure in the region.

**Key words:** galaxies: clusters: individual (Abell 3667) — galaxies: magnetic fields — radiation mechanisms: non-thermal — X-rays: galaxies

## 1. Introduction

Enigmatic extended radio sources in rich galaxy clusters have been known for over 30 years (Willson 1970; for recent review, see L. Feretti 2005<sup>1</sup>). Sources located at the cluster

center are referred to as “radio halos”, while those on the cluster periphery are called “relics”. Steep spectra and spectral cutoffs at a few GHz detected in several halos/relics indicate that relativistic electrons with typically GeV energy are undergoing cooling due to synchrotron and inverse Compton (IC) emissions. In every case, the radio halos/relics are found in irregular clusters that are apparently undergoing mergers. This

<sup>1</sup> Feretti (2005) is available at (<http://www.aoc.nrao.edu/events/xraydio>), in X-Ray and Radio Connections, ed. L. O. Sjouwerman & K. K. Dyer, 10.

suggests that the radio emitting electrons are accelerated by shocks or turbulence generated by energetic cluster merging.

The same relativistic electrons scatter Cosmic Microwave Background (CMB) photons up to the hard X-ray band (IC emission). By comparing the radio and the hard X-ray emissions, not only the electron energy density, but also the intra-cluster magnetic field intensity can be estimated (e.g., Sarazin 1986). Detecting the IC emission is difficult because of the strong ICM component dominant below  $\sim 20$  keV and the low expected flux of the emission in hard X-rays above this energy. Currently, there are only a few reports claiming its detection, mostly from the Beppo-SAX PDS in the energy band around 40 keV or higher (e.g., Fusco-Femiano et al. 1999; Nevalainen et al. 2004), though a few of the detections are still controversial (Rossetti & Molendi 2004; Fusco-Femiano et al. 2007). There are reports from RXTE (e.g., Petrosian et al. 2006; Rephaeli et al. 2006) as well. Another case includes the ASCA GIS results around 4 keV on galaxy groups (Fukazawa et al. 2001; Nakazawa et al. 2007). These results would require a magnetic field as low as  $0.1 \mu\text{G}$  (e.g., Fusco-Femiano et al. 1999), which at first glance is inconsistent with the radio rotation measure estimation of  $2\text{--}10 \mu\text{G}$  (e.g., Clarke et al. 2001; Carilli & Taylor 2002). Further observations by independent instruments of IC and other hard X-ray emission processes (e.g., Inoue et al. 2005) are thus desirable.

Significant heating of the ICM, itself, must also be taking place in merging clusters (e.g., Takizawa 2000; Ricker & Sarazin 2001). X-ray hardness ratio images sometimes show temperatures exceeding 10 keV (e.g., Watanabe et al. 1999; Briel et al. 2004). Since the emission can be multi-phase phenomena within the line of sight, the actual highest temperature can be much higher, though it is not easy to identify using the contemporary imaging X-ray detectors working below 12 keV.

In many ways, Abell 3667 is an ideal cluster to study mergers, radio relics, and hard X-ray emission. It is a very bright X-ray cluster at a low redshift of  $z = 0.0556$  (Struble & Rood 1999). The ROSAT and ASCA observations showed that it is a spectacular merger with shock-heated gas (Markevitch et al. 1999). Chandra and XMM-Newton observations have shown much evidence for an ongoing merger, such as a cold front (Vikhlinin et al. 2001a, 2001b) and a highly inhomogeneous temperature structure with temperature ranging from 4 to  $> 10$  keV (Mazzotta et al. 2002; Briel et al. 2004). The optical galaxy distribution shows elongation towards the northwest-southeast axis (Sodre et al. 1992; Johnston-Hollitt et al. 2008), supporting the binary merger scenario as well.

The cluster is famous for its pair of radio relics (e.g., Röttgering et al. 1997). The relic to the north-west is the brightest and largest among the diffuse radio sources associated with the cluster of galaxies, having a flux of 3.7 Jy (Johnston-Hollitt 2004) and a width of  $\sim 20'$  at 1.4 GHz. It is located about  $30'$  or 2 Mpc from the cluster X-ray centroid. The radio signal is detected from 85 MHz to 2.3 GHz, and its average photon index is  $\Gamma = 2.1$  (Röttgering et al. 1997). Here, the photon index,  $\Gamma$ , is defined as  $N_{\text{photon}}(E) = N_0 \times E^{-\Gamma}$ . The radio relics have very sharp outer edges, and the radio spectra steepen with distance from the edge. Thus, the radio relics are considered to reflect the position of the particle acceleration

**Table 1.** Log of the three Abell 3667 observations.

Name	Start (UT)	End (UT)	Exposure*
NW_Relic	05/03 17:47	05/06 07:02	81.2/45.6
NW_17off	05/06 07:03	05/06 17:39	16.7/11.4
Center	05/06 17:40	05/07 09:13	20.5/ 7.2

\* The XIS/HXD exposure time in ks after the screening as presented in the text.

in a merger shock. The cluster is also a good candidate for the detection of IC emission. The Beppo-SAX PDS provided rather marginal evidence of hard excess emission from the cluster (Fusco-Femiano et al. 2001; Nevalainen et al. 2004). However, the large field of view (FOV) of the PDS makes the data strongly affected by contamination from thermal emission from the entire cluster, mainly from its central region, and possible AGNs.

The hard X-ray detector (HXD: Takahashi et al. 2007; Kokubun et al. 2007) onboard Suzaku (Mitsuda et al. 2007) is characterized by its low detector background in the 10–40 keV band and its narrow FOV of  $34'$  in full width at half maximum (FWHM). Using the HXD, we can spatially distinguish hard X-ray components from the cluster center and the north-west relic, with the highest sensitivity in the 10–40 keV band. In addition, the X-ray CCD cameras (XISs: Koyama et al. 2007) onboard Suzaku are characterized by their large effective areas and low and stable detector backgrounds, which make them very powerful devices to observe extended hard emission.

In 2006 May, we observed the Abell 3667 cluster using Suzaku with three pointings running from the north-west relic to the center, each separated by  $\sim 17'$ . Here, we report on results obtained by these observations. Observation logs and data reduction are described in the next section. Section 3 is devoted to spectral and imaging analyses, followed by a discussion in section 4 and conclusions in section 5. In this work, we utilized a canonical cosmology value of  $H_0 = 70 \text{ km s}^{-1} \text{ Mpc}^{-1}$ . At a redshift of  $z = 0.0556$ ,  $1'$  corresponds to 62 kpc. For a mean cluster temperature of 7.2 keV, the virial radius should be  $r_{200} \sim 2.6 \text{ Mpc} = 42'$  (e.g., Neumann & Arnaud 1999). Unless otherwise noted, all errors are at the 90% confidence limit.

## 2. Observation and Data Reduction

### 2.1. Observation Logs

Three Abell 3667 pointing observations of Suzaku were carried out successively in the beginning of 2006 May. As already noted, individual pointing positions were offset by  $\sim 17'$ , so that the first observation covered the north-west relic, and the last one on the cluster center, with continuous XIS coverage. Hereafter, we call these observations the NWR, the  $17'$  offset and the center pointing, respectively. Details of the observation times are summarized in table 1. The FOVs of individual pointings compared with the X-ray sky image of PSPC are also presented in appendix 3.

The XIS was operated in the normal timing and the full window mode. All of the 64 PINs of the HXD were operated in the nominal bias voltage of 500 V. All of the data were processed with the Suzaku pipeline processing

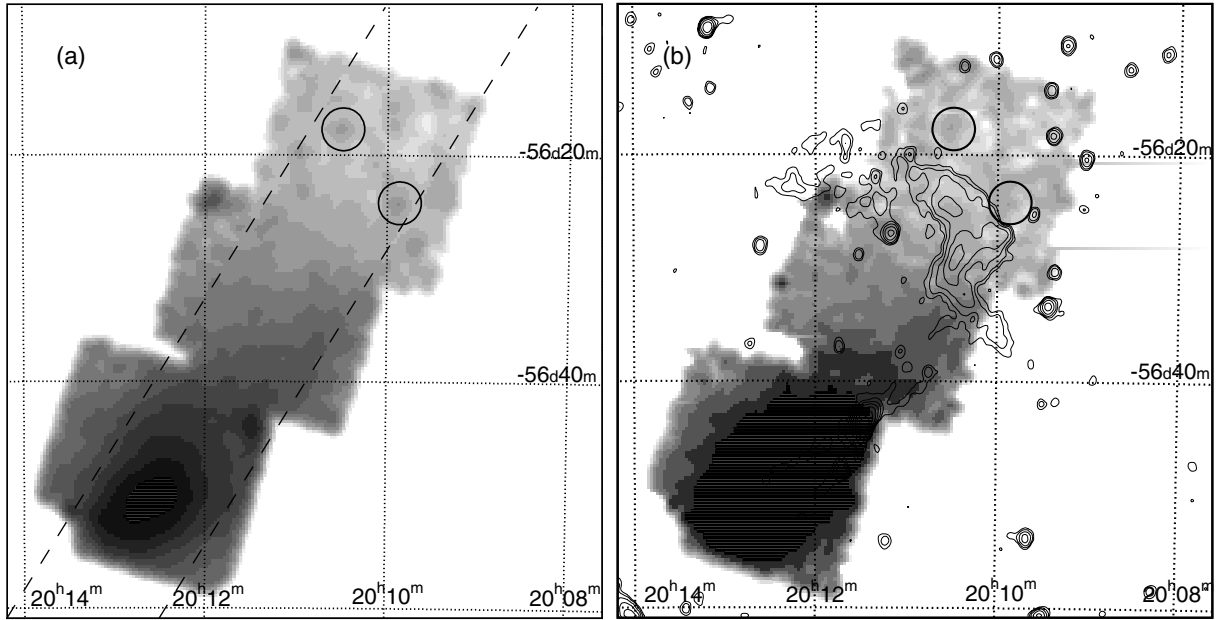


**Fig. 1.** Mosaic XIS image of the three pointing observations, in (a) the soft 1–4 keV band and (b) the hard 4–8 keV band. See text for details. The images were smoothed by a Gaussian kernel with  $\sigma = 0.5$ . Gray-scale contours were logarithmically scaled by a factor of 1.5. In the hard band image, the 843 MHz radio image (by SUMSS) is overlaid as a thin contour. Two point source candidates are shown as open circles in the NWR region, and the projection analysis band is shown as a dashed lines in panel (b); both are discussed later in sub-subsection 3.4.3.

of version 2.0.6.13.

## 2.2. Data Reduction of the XIS

### 2.2.1. Screening and background estimation

The XIS data were processed via default screening criteria. Events with GRADE of 0, 2, 3, 4, 6, and STATUS < 1024 were extracted. Data-screening criteria with HK files were as follows: time after SAA (T.SAA.HXD) > 436 s, new cut-off rigidity (COR2) > 6.0 GV, elevation from the Earth rim > 5° and that from the Sun-lit Earth rim > 20°. Non-X-ray background (NXB) spectra of the XIS were created by sorting night Earth data by COR2, and weighted-averaging them using the ftool “xisnxbgen” (Tawa et al. 2008). The estimation uncertainty in the NXB level was handled as a systematic error in the following analysis. Tawa et al. (2008) studied the error on a typical observation lasting for a few days. At the 90% confidence level, it was 6.0% and 12.5% for the sum of three XIS-FI (XIS-0,2,3) data and the BI (XIS-1) data, respectively.

Another major background is the Cosmic X-ray background (CXB). Details of the CXB estimation are given in appendix 1. Because the whole XIS region in all the three observations could be filled with non-thermal or thermal diffuse emission, we used the Lockman Hole observation (Suzaku observation ID, 101002010) as the CXB template. In addition, the northern 1/3 of the NWR pointing data was utilized for foreground Galactic soft thermal component modeling. The CXB fluctuation was estimated to be 11% over the XIS full FOV. Hereafter, we treat the background-subtracted (both the NXB and CXB) spectra as signals from Abell 3667.

### 2.2.2. The XIS image

In figure 1, we show 1–4 keV and 4–8 keV XIS-FI mosaic images of the three pointings. After co-adding the images from XIS-0, 2, and 3, they were corrected for the overlapping

exposure, and for a vignetting effect of the mirror optics, after subtracting the NXB. Thanks to the wide energy range and low background of the XIS, we can see signals even in the NWR region, which is 30′ (2 Mpc) away from the X-ray centroid. On the other hand, no apparent emission associated with the radio relic is seen in either band image. A detailed analysis using these images is described in sub-subsection 3.4.3.

## 2.3. Data Reduction of the HXD

### 2.3.1. Screening and background estimation

We processed the uncleaned event files of the HXD with “hxdgtigen”, and remaining events were further screened with HK files as follows: time after SAA (T.SAA.HXD) > 500 s, the COR2 > 8.0 GV, and elevation from the earth rim > 5°. As the NXB of the PIN, we utilized a public NXB model, which was provided by the HXD team on the Suzaku website.<sup>2</sup> The version of the model was “METHOD = LCFITDT”, or “tuned”. Observations of Abell 3667 were carried out during a period in which the lower threshold of the scintillator was set to be low, and a data transfer overflow between the HXD’s analog and the digital electronics sometimes occurred. These phenomena should not take place in ordinary observations, and hence corresponding time regions were discarded in the default screening criteria. In fact, the effect of this phenomena in principle is recoverable through a dead-time correction procedure, and thus the data should be useful. Since the HXD data in this paper, however, are dominated by systematic errors, and not statistics, and most of the systematic error analysis is performed during periods excluding these phenomena, we stuck to the original screening criteria. Note that none of the results were changed significantly if we included the data

<sup>2</sup> (<http://www.astro.isas.jaxa.jp/suzaku/analysis/hxd/pinnxb/>).

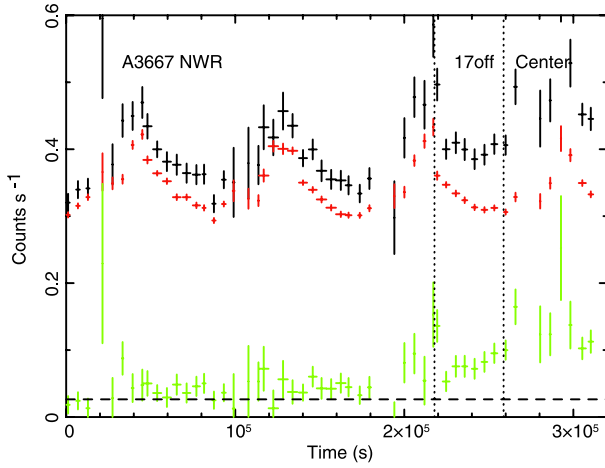


**Fig. 2.** HXD light curves in the 13–40 keV range. Black crosses stand for the data, red for the background model, and green for the residual signals. Time regions of the three observations are separated by vertical dotted lines. The horizontal dashed line indicates the expected CXB rate.

obtained during periods with data transfer overflow.

In the HXD-PIN NXB documents (Fukazawa et al. 2009; Mizuno et al. 2008<sup>3</sup>), the reproducibility of blank-sky observations separated into 10 ks exposures gave a distribution of 5.7% at the 90% confidence level, including the statistical error, typically 3.3% or larger, and a CXB fluctuation of 1.3%, as described later. This gave a NXB systematic uncertainty of 4.5% at the 90% confidence. In a following analysis, we utilized this value as the systematic error of the NXB. Because the selection criteria of the blank-sky observations are simple and based only on the XIS source flux, some of them can be contaminated by off-center sources. In addition, 10 ks is slightly shorter than the exposure of our observations. Thus, the actual systematic error is probably smaller than this value.

Details of the CXB model used for the PIN are described in appendix 2. We defined the photon flux model as  $N(E) = 8.69 \times 10^{-4} \times E^{-1.29} \times \exp(-E/40.0)$  in photons  $\text{cm}^{-2} \text{s}^{-1} \text{keV}^{-1} \text{FOV}^{-1}$ . Here,  $E$  is the photon energy in keV, and the model was normalized to the HXD-PIN opening angle (or FOV) of  $\Omega_e^{\text{HXD}} = 0.32 \text{ deg}^2$ , to be combined with the HXD nominal response. The 13.2% systematic difference of the XIS and PIN (M. Ishida et al. 2007)<sup>4</sup> was also accounted in a following fitting process. The level of the CXB fluctuation was calculated to be 18%, which corresponds to 1.3% of the CXB + NXB in the 10–40 keV band.

We also checked whether the PIN data suffered from thermal noise in the lower energy band by comparing the actual Earth occultation data with the corresponding model NXB spectra. Since the detector temperature was relatively high at  $-12^\circ\text{C}$  in these observations, the thermal noise was seen as a steep rise below 13 keV. In the higher energy band, the two spectra are consistent within statistics.

### 2.3.2. Signals of the three pointings

In figure 2, the 13–40 keV band light curves of PIN for a total of 4 days of observations are presented. The PIN

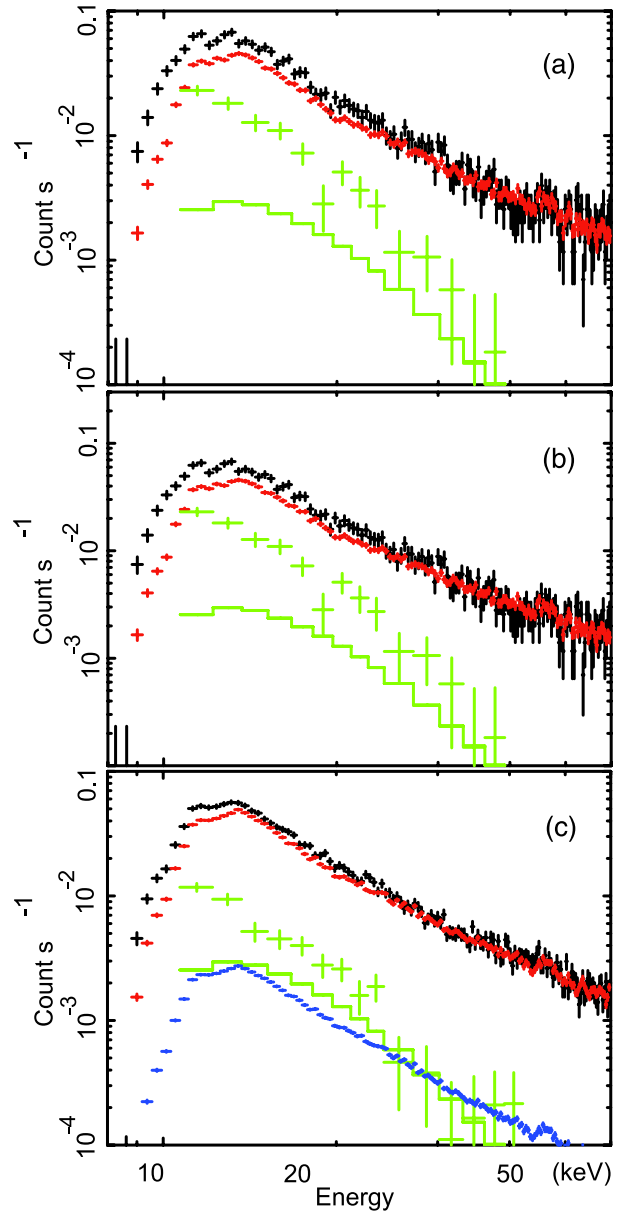


**Fig. 3.** PIN spectra of the three pointings, from (a) center, (b) 17' off, and (c) NWR. Black crosses stand for the data, red for the NXB model, and green for the residual signals (data – NXB). The expected CXB spectra are also plotted as green histograms. Typical systematic errors due to the CXB fluctuations and the NXB reproducibility are shown in the NWR data in blue.

background varies by  $\sim 25\%$ , mainly correlated with COR, and time elapsed after a passage of SAA (T\_SAA\_HXD). The PIN residual signal clearly exceeds the CXB level for all three observations. Note that the flux increases towards the cluster center. Small variations seen in the residual signal are due to uncertainties in the NXB modeling in this rather short time bin (90 minutes), and the NXB-subtracted count rate is consistent with being constant within each pointing.

In figure 3, we show raw PIN spectra from the 3 observations, together with the NXB model spectra. Difference between the two spectra are also presented, and compared

<sup>3</sup> JX-ISAS-SUZAKU-MEMO-2008-03.

<sup>4</sup> JX-ISAS-SUZAKU-MEMO-2007-11.

to the CXB model. In all cases, the NXB-subtracted data significantly exceeds the CXB. The signal was strongest in the center pointing, and weakest in the NWR pointing. The 13–40 keV PIN signal rates were  $(8.9 \pm 1.3, 5.4 \pm 1.0, \text{ and } 1.4 \pm 0.5) \times 10^{-2} \text{ counts s}^{-1}$  in the center, the 17' offset, and the NWR data, respectively. The systematic error was  $1.5 \times 10^{-2} \text{ counts s}^{-1}$  in all pointings, when evaluated as a quadrature sum of those of the CXB and the NXB. Thus, we can claim signal detection from Abell 3667 up to 30 keV both in the center and 17' offset observations.

We also estimated the point-source contribution to the HXD-PIN using the ROSAT-PSPC and the ASCA-GIS data. In short, we confirmed that the contribution from these sources was less than 10%, and hence almost negligible. Details are given in appendix 3.

#### 2.4. Preparation of arf Files of the XIS and the PIN

When trying to quantify the brightness and spectral shape of the PIN signals, we need to know the angular transmission (or effective area) of PIN to the corresponding hard X-ray emission. This in turn requires knowledge of the location and shape of the source, which is unavailable in the PIN energy range. In evaluating the ICM contribution to the PIN band, we therefore assumed it to have the same spatial distribution as the ICM signals detected with the PSPC. Here, the ICM was assumed to be isothermal, which is not completely true for this cluster. However, this assumption is valid as a starting point, since the major part of the ICM emission contributing to the PIN band originates from within 20' of the cluster center, within which region the average spectra is well approximated by a  $\sim 7$  keV ICM emission (see sub-subsection 3.1.1 and subsection 3.2). In this case, inhomogeneity in the ICM spectra is observable as a small shift in spectra of individual pointings.

The PSPC image was background subtracted and corrected for the vignetting effects following the method described in Snowden et al. (1994). Since the ICM emission in the image is not observable beyond 40' from the cluster center, we discarded the data in this region. After normalizing the image to have a total area of 1.0 and binning it with a  $2' \times 2'$  mesh, we simply calculated the PIN arf file by convolving the point source arf of the specified mesh multiplied by its relative intensity. Note that the energy response in principle has a negligible dependence on the position within the PIN-FOV. The cross-normalization factor of 1.132 between the PIN and the XIS was incorporated, as well.

Regions beyond 26' from the cluster center, i.e., those as far as the XIS FOV of the NWR pointing, contributed only 1.3%, 4.9%, and 14.4% to the normalization of arf files of the center, the 17' offset and the NWR pointings, respectively. Thus, 86% of the ICM photon detected in the NWR PIN data is expected to come from the inner region of the cluster. Interestingly, the normalization relative to the center pointing thus calculated are 0.61 and 0.14 in the 17' offset and the NWR pointings, respectively. These values match the actually observed ratios,  $0.60 \pm 0.25$  and  $0.11 \pm 0.18$ , respectively. As a reference, those of a point source located at the cluster X-ray centroid are 0.42 and 0.05, respectively. These results suggest that the ICM emission around the cluster central region must be carefully handled when analyzing the NWR PIN data.

In a similar way, we synthesized the XIS arf files with the ftool “xissimarfgen”, using the PSPC image as an input. Note that the input image is automatically normalized to 1.0 in the software. Thus, the spectral fitting of both the PIN and the XIS was normalized to the whole cluster, and not the FOV of each detector of individual observations. Since the NWR region is around the detection limit of both the PSPC and the XIS, the arf files for this region could be inaccurate, and they require special care in the following analysis. This effect is negligible in the center and 17' offset pointings because of the high X-ray surface brightness.

To verify the accuracy of the generated arf files, we compared the XIS results to those of the PSPC. We derived the 0.5–2.0 keV ICM flux by integrating the PSPC surface brightness profiles given by Mohr et al. (1999) within 40' from the X-ray centroid. The value matched within 1% to the flux obtained by fitting the center XIS FI spectra using our arf, which was also normalized to the PSPC image integrated over 40'. Here, a  $kT = 7$  keV single temperature thermal emission was assumed. Although the analysis described in this paper was not sensitive to the Suzaku-PSPC cross calibration, this result supports our arf generation procedure. On the other hand, the XIS and PIN cross-calibration, to which our analysis was sensitive, was verified within  $\sim 3\%$  accuracy using Crab observations, including mapping within the PIN-FOV. Because the PIN-FOV is relatively simple in its shape, no strong systematic error is expected. Using a similar approach, the PIN spectra of the Abell 1060, Centaurus (T. Kitaguchi private communication), and Coma clusters (Wik et al. 2009) were successfully reproduced by extrapolating the XIS or XMM spectra. From these results, we conservatively assume a 10% uncertainty in the *relative* normalization of the XIS and the PIN arf files.

### 3. Wide-Band Spectral Analysis

#### 3.1. Spectral Properties of the Central Pointing

With the preparation made in section 2, we proceed to the spectral analysis of the XIS and the PIN. The central pointing afforded signal detection with the highest significance using both instruments. Their arf files are also the most reliable, since the brightest central emission is well detected by the PSPC. Thus, we started the spectral fitting from the central pointing. We first evaluated the XIS and the PIN spectra individually, and then performed a combined fitting.

Spectra from the three XIS-FI chips were summed up to form a single XIS-FI spectrum. Since the XIS-BI chip has a significantly different detector response, its spectra was separately handled. The arf files prepared in subsection 2.4 were used for the XIS-FI, XIS-BI, and the PIN data. Thus, the normalization of individual spectra should be the same. Practically, we fixed the relative normalization between the XIS-FI and the PIN data, and the 10% systematic uncertainty was handled separately. The normalization between the XIS-FI and BI data was set free so as to adjust for residual mutual calibration uncertainties of about 5% or less. Here, the XIS-FI, the XIS-BI, and the PIN spectra were utilized in 0.6–10.0 keV, 0.6–8.0 keV, and 13–40 keV, respectively. Since the data had very high statistics, the energy range of 1.76–1.86 keV in the

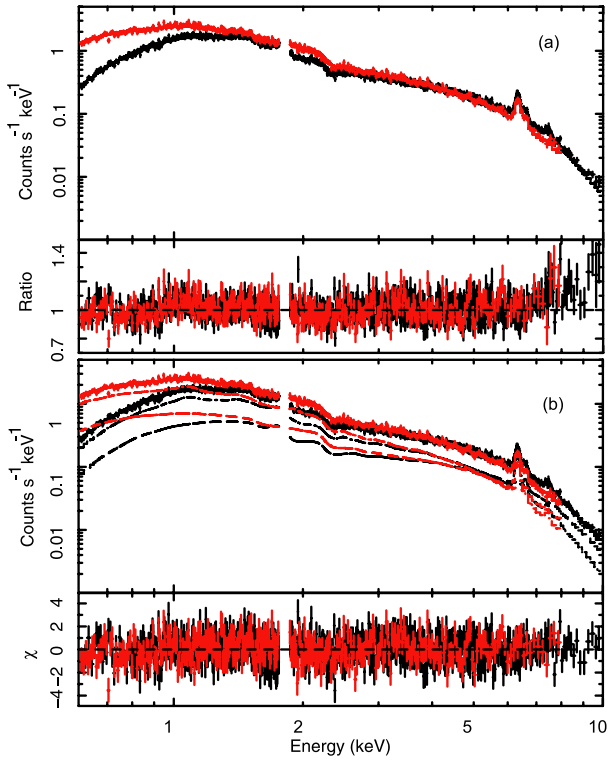


**Fig. 4.** XIS-FI (black) and XIS-BI (red) center spectra, fitted with (a)  $1kT$  and (b)  $2kT$  thermal emission models. In panel (b), two thermal components are independently presented as dashed histograms.

XIS spectra was ignored so as to avoid uncalibrated structures caused by the Si edge. The XIS-FI and BI spectra are grouped so that each energy bin has at least 200 counts. The PIN spectra are grouped into 12 fixed bins, each with sufficient counts.

### 3.1.1. The XIS

We first applied a single temperature thermal emission model (hereafter  $1kT$  model) to the XIS spectra, utilizing the *apec* code in the XSPEC (v11.3.2) software package. Galactic absorption was modeled by the *wabs* code with a fixed column density of  $4.7 \times 10^{20} \text{ cm}^{-2}$ , as derived by the radio observations (Dickey & Lockman 1990). The redshift was also fixed at  $z = 0.0556$ . The relative ratio of the metal abundances are fixed to the solar value, given by Anders and Grevesse (1989). The temperature and the normalization were also set free.

A fit with the  $1kT$  model was unsuccessful with a  $\chi^2/\text{d.o.f.} = 1139.6/1004$ , leading to a null hypothesis probability of  $1.8 \times 10^{-3}$ . The fitted temperature was about 6.8 keV, which is generally consistent with temperatures given in the literature (e.g., Fukazawa et al. 2004). Figure 4 presents the data compared to the best-fit model. In the  $1kT$  fitting, residuals around 1 keV and above 8 keV are significant. Even if we set the  $N_{\text{H}}$  free, the fit did not improve significantly, suggesting the thermal component modeling itself needs improvement.

Considering the multi-temperature nature of the cluster (e.g., Briel et al. 2004), we added another thermal component (table 2). The metal abundances of the two *apec* components were tied to be the same, and only the temperature and normalization were set free (hereafter  $2kT$  model). The fit

**Table 2.** Best parameters of the models fitted to the center XIS spectra.

	$1kT$	$2kT$
$kT_{\text{low}}^*$	6.8	$4.71^{+0.27+0.07}_{-0.34-0.06}$
$kT_{\text{hi}}^\dagger$	—	$22.3^{+7.5+1.1}_{-5.0-1.4}$
$Z^\ddagger$	0.32	$0.38^{+0.03+0.01}_{-0.03-0.00}$
$N_{\text{low}}^\S$	$9.5 \times 10^{-2}$	$6.4^{+0.6+0.0}_{-0.8-0.1} \times 10^{-2}$
$N_{\text{hi}}^\S$	—	$3.5^{+0.6+0.1}_{-0.5-0.1} \times 10^{-2}$
$\chi^2/\text{d.o.f.}$	1139.6/1004	1035.4/1002

\* Temperature of the (cooler) thermal component in the  $1kT$  ( $2kT$ ) fit, in keV. Errors are 90% statistical and systematic, respectively, latter evaluated by shifting the NXB and CXB within their systematic errors.

† Temperature of the hotter thermal component in the  $2kT$  fit.

‡ Metal abundance.

§ Normalization in the *apec* code, for the low and high temperature components.

significantly improved and became acceptable with  $\chi^2/\text{d.o.f.} = 1035.4/1002$  or a null hypothesis probability of 23%. Here, we also estimated the systematic error by shifting both the NXB and CXB to their highest and lowest possible values at the 90% confidence. The shifts observed in the fitted central value were quoted as systematic uncertainty. In this fitting, the hotter component temperature is suggested to be higher than 17.1 keV. Here (and in all of the following analysis), the errors were derived as a quadrature sum of the statistical and the systematic ones when obtaining the final result, while the two components are separately presented in the tables for clarity. When fitted using a model with thermal and power-law components (hereafter  $1kT + \text{PL}$  model), the fit also improved, providing  $\chi^2/\text{d.o.f.} = 1057.8/1002$  or a null hypothesis probability of 10.1%. The photon index derived is hard with  $\Gamma = 1.0^{+0.2}_{-0.8}$ . Before further modeling the ICM, we will check the HXD-PIN spectra, since it should contain information about hotter or harder components.

### 3.1.2. The HXD-PIN

The signal detected by the PIN is significant compared to any possible systematic errors. We then studied the shape of the PIN spectrum in the 13–40 keV range. Here, we used the HXD nominal position response, and have not yet used the arf files generated at subsection 2.4. When we simply fit a power-law model to the PIN spectrum, the resultant photon index,  $\Gamma$ , was as soft as  $3.6^{+1.1}_{-0.9}$ . If we tried the  $1kT$  model with metal abundances fixed at 0.3, the resultant temperature was derived as  $8.5^{+5.8}_{-3.4}$  keV. Detailed results are presented in table 3. At first glance, no strong signature of a spectrally hard component is suggested in the PIN spectra. We also note that, although the error bar is large because of both statistical and systematic errors, the photon index,  $\Gamma$ , is softer than those, suggested from the radio observation, i.e.,  $\Gamma \approx 2.1$  and the XIS spectral fitting with  $1kT + \text{PL}$  model. On the other hand, the PIN flux level provides important results, as shown in the next section.

### 3.1.3. Combined XIS-HXD analysis

Following spectral analyses individually performed to the XIS and the PIN, in this section we give the results of a wide-band spectroscopic analysis, using the two spectra combined

**Table 3.** Spectral parameters fitted to the HXD spectra.\*

Model	$\Gamma$ or $kT$ <sup>†</sup>	Flux or norm <sup>‡</sup>	$\chi^2/\text{d.o.f.}$
PL	$3.6^{+1.0+0.5}_{-0.8-0.3}$	$32^{+5+6}_{-5-6}$	6.2/10
$1kT$	$8.5^{+5.6+1.6}_{-2.9-1.8}$	$7.8^{+12.1+2.2}_{-4.1-1.0}$	6.2/10

\* Center pointing in the 13–40 keV range.

<sup>†</sup> Photon index  $\Gamma$  or thermal component temperature (in keV) of the power-law or  $1kT$  fitting, respectively.

<sup>‡</sup> The 10–40 keV flux of the power-law component, in  $10^{-12} \text{ erg s}^{-1} \text{ cm}^{-2}$ , or the normalization in *apec* model, for the low and high temperature components.

(the XIS + PIN combined spectra). In order to connect the two instruments and derive the ICM component, we utilized the arf files generated in subsection 2.4, and fixed the normalization of the XIS-FI and the PIN spectra.

We first applied the  $1kT$  model. The procedures and fitting parameters were the same as those of the XIS-only analysis. The fit again gave a temperature of  $\sim 6.9$  keV. However, as shown in figure 5a, the  $1kT$  model failed to explain the PIN data, as well as the XIS data in the energy band above 7 keV. As a result, the fit was unacceptable with  $\chi^2/\text{d.o.f.} = 1173.4/1016$ . What is more, the observed PIN counts were about a factor of 2 larger than the best-fit  $1kT$  model. This excess is larger than any possible calibration errors in the arf, and any systematic error associated with the NXB and CXB, as well.

To characterize the hard excess, we next applied the  $2kT$  model. The relative normalizations of the two components were the same in the XIS and the HXD-PIN spectra. In other words, we assumed a simple model in which the ICM emission uniformly contained the two components. Since 75% of the ICM emission accumulated in the center PIN data came from within  $12.5'$  from the X-ray centroid, which is mostly covered by the center XIS FOV, this model is valid as a simple approximation. As shown in figure 5b and table 4, a good fit with  $\chi^2/\text{d.o.f.} = 1046.5/1014$  or a null-hypothesis probability of 23.3% was obtained. Interestingly, both the XIS and the PIN hard excess *consistently* disappeared. Considering both the statistical and systematic errors (table 4), this hard component, if interpreted as thermal, is characterized by a temperature of  $kT_{\text{hi}}$  ranging from 13.2–25.8 keV.

As another candidate, we fitted the  $1kT + \text{PL}$  model to the XIS + PIN combined spectra. The fit was improved compared to the  $1kT$  model, and marginally acceptable, giving 4.8% in null hypothesis probability. As shown in table 4, the photon index was hard with  $\Gamma = 1.4$  and the inferred power-law flux in 10–40 keV was  $\sim 4 \times 10^{-11} \text{ erg s}^{-1} \text{ cm}^{-2}$ , normalized to the cluster as a whole.

The  $2kT$  model is the simplest one to evaluate the multi-temperature nature of the cluster ICM. We thus also tried a model with three *apec* components (hereafter  $3kT$  model). In this case, we fixed one of the three temperatures to 7.5 keV to make the fit converge. The value refers to the  $1kT$  fit to the  $17'$  offset data shown in the next section, and is also consistent with one of the major components seen in the XMM mosaic (Briel et al. 2004). As shown in table 5, the fit was acceptable with a null hypothesis probability of 27%. A hot component

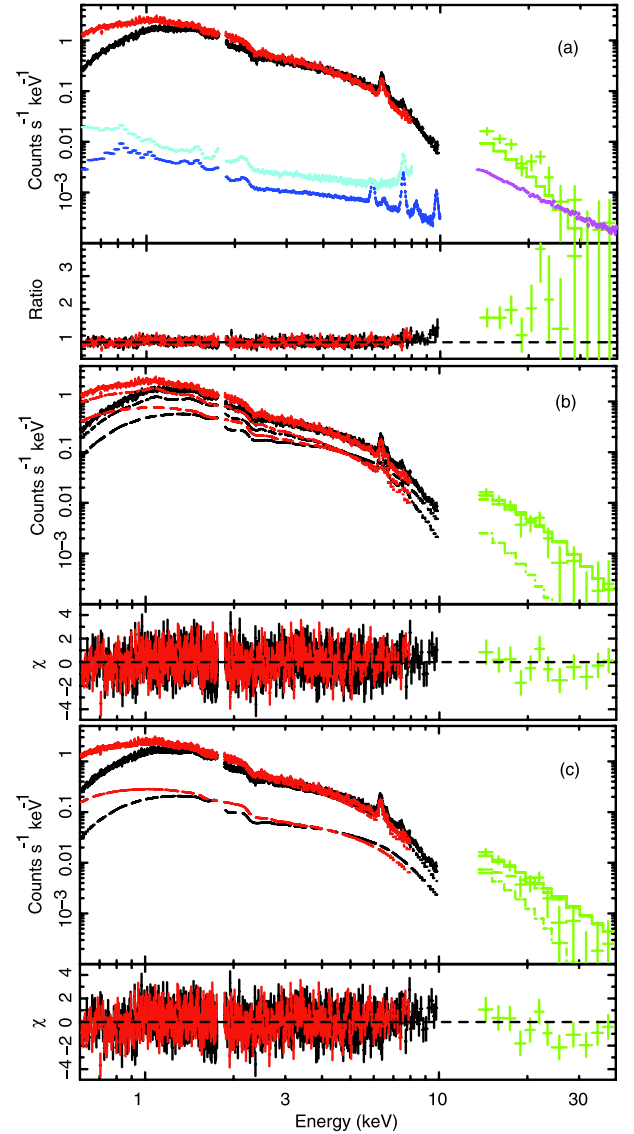


**Fig. 5.** Wide-band spectra of the center pointing, fitted with the (a)  $1kT$ , (b)  $2kT$ , and (c)  $1kT + \text{PL}$  models. In the panel (a), typical 90% confidence systematic error in the NXB and CXB are also shown for reference, in cyan, blue, and magenta corresponding to the XIS-FI, BI, and PIN, respectively. Panel (a) is shown together with the residual ratio, while the other two are with the delta-chi distribution.

with a temperature  $kT_{\text{hi}} = 27.3^{+\infty}_{-8.2}$  keV is required, but with  $\sim 40\%$  smaller normalization compared to those of the hotter component of the  $2kT$  model. If we shifted the temperature ranging from 6.5 to 8.0 keV, the fit was still acceptable, and the parameter value was generally similar. In other words, we still needed a component as hot as  $\sim 20$  keV, which could also be replaced by a  $\Gamma \sim 1.4$  power-law component.

The temperature map derived from XMM mosaic shows several hot regions with  $kT > 8$  keV around a few minutes north-west to the X-ray centroid (see figure 2 of Briel et al. 2004). Using Chandra, the signature of a component as hot as  $> 10$  keV is also suggested in the same region (A. Vikhlinin et al., private communication). Due to the projection of emission components, these value should be regarded as a lower

**Table 4.** The best fit parameters of the  $2kT$  and  $1kT + \text{PL}$  models.\*

	$2kT$	$1kT + \text{PL}$
$kT_{\text{low}}$	$4.69^{+0.29+0.01}_{-0.40-0.08}$	$6.05^{+0.18+0.24}_{-0.20-0.28}$
$kT_{\text{hi}}$	$19.2^{+4.7+4.6}_{-4.0-4.5}$	—
$Z$	$0.39^{+0.03+0.00}_{-0.03-0.01}$	$0.35^{+0.03+0.01}_{-0.03-0.01}$
$N_{\text{lo}}$	$6.1^{+0.6+0.2}_{-0.8-0.4} \times 10^{-2}$	$8.2^{+0.5+0.5}_{-0.4-0.3} \times 10^{-2}$
$N_{\text{hi}}$	$3.6^{+0.8+0.4}_{-0.6-0.0} \times 10^{-2}$	—
$\Gamma_{\text{PL}}^\dagger$	—	$1.39^{+0.10+0.00}_{-0.17-0.02}$
$F_{\text{PL}}^\ddagger$	—	$37^{+7+14}_{-6-13}$
$\chi^2/\text{d.o.f.}$	1046.5/1014	1089.8/1014

\* Fitted to the XIS + PIN combined spectra of the center pointing. Columns are similar to those shown in table 2. The systematic error includes the XIS-PIN arf uncertainty of 10%, in addition to those of the CXB and NXB.

† Photon index of the power-law component.

‡ 10–40 keV flux of the power-law component, in  $10^{-12} \text{ erg s}^{-1} \text{ cm}^{-2}$ .

**Table 5.** Best-fit parameters of the  $3kT$  model.\*

	$3kT$
$kT_{\text{low}}$	$3.68^{+0.56+0.00}_{-1.14-0.86}$
$kT_{\text{med}}^\dagger$	7.5 (fixed)
$kT_{\text{hi}}$	$27.3^{+\infty+\infty}_{-8.2-0.0}$
$Z$	$0.38^{+0.02+0.00}_{-0.02-0.02}$
$N_{\text{lo}}$	$3.0^{+1.5+0.0}_{-1.6-1.4} \times 10^{-2}$
$N_{\text{med}}$	$4.7^{+2.5+2.3}_{-2.5-0.0} \times 10^{-2}$
$N_{\text{hi}}$	$2.1^{+1.1+0.0}_{-1.1-1.1} \times 10^{-2}$
$\chi^2/\text{d.o.f.}$	1046.5/1014

\* Fitted to the XIS + PIN combined spectra of the center pointing.

† A fixed temperature of the medium hot component.

limit, and thus a very hot ( $> 13.2$  keV) component is apparently required in the cluster. In following analyses, we regarded the  $2kT$  model as an upper limit of the ICM contribution to the PIN-band, which is the most important issue in this paper. Using additional long-exposure XMM data to be obtained soon, we will further pursue this issue in the next paper.

Through these analyses, we conclude that the excess hard component suggested in the XIS data is clearly required in the PIN spectra as well. The emission is likely to be of thermal origin, a very hot component with temperature exceeding 13.2 keV, or less likely a hard ( $\Gamma \sim 1.5$ ) power-law component. We also checked the Fe-K line profile, and found that it was consistent with either the  $1kT + \text{PL}$ ,  $2kT$ , and  $3kT$  interpretations. In any case, analyses of the other observations, i.e., the 17' offset and the NWR pointings, will be helpful to identify the origin of the hard emission. The XIS and PIN data in these pointings contain spatial information on the excess component. What is more, the strong north-west radio relic was observed with the deep (81 ks in the XIS) NWR pointing.

### 3.2. Spectral Properties of the Offset Pointings

When analyzing the offset pointings, we have to take into account that, although the XIS spectra are of local origin (from

**Table 6.** Best parameters for the 17' off and the NWR offset spectra.\*

	17' off <sup>†</sup>	NWR <sup>‡</sup>
$kT$ (keV)	$7.71^{+0.33+0.38}_{-0.32-0.47}$	$3.6^{+0.4+0.5}_{-0.4-0.6}$
$Z$	$0.26^{+0.06+0.01}_{-0.06-0.01}$	$0.16^{+0.16+0.01}_{-0.14-0.00}$
$N^\S$	$9.3^{+0.2+0.1}_{-0.2-0.2} \times 10^{-2}$	$7.4^{+0.6+1.2}_{-0.5-1.6} \times 10^{-2}$
$\chi^2/\text{d.o.f.}$	234.1/220	120.5/89

\* Fitted with the  $1kT$  model.

† Fitted to the XIS + PIN combined spectra.

‡ Fitted only to the XIS spectra.

§ Normalization in *apec* model. Note that it is normalized to the whole cluster, not within the observation FOV, using the arf files generated from the PSPC image.

within the FOV), the PIN spectra is largely contaminated from the emission from the cluster center. For example, 59% and 37% of the ICM emission accumulated in the 17' offset and the NWR pointings, respectively, comes from within 12.5 from the X-ray centroid, i.e., around the center. Therefore, the XIS and the PIN spectra will not necessarily show the same results, although they should be roughly consistent with one another as a whole.

The XIS spectra of the 17' offset pointing can be represented using the  $1kT$  model, with  $kT = 7.6^{+0.4}_{-0.4}$  keV and  $\chi^2/\text{d.o.f.} = 221.9/208$ , or a null hypothesis probability of 24.3%. Note that we utilized the arf files generated in subsection 2.4 so that the (energy dependent) vignetting effect is fully taken into account. For the same reason, the fitted flux was normalized to the reference image used in the arf generation (in this case the whole cluster), not just the flux within the FOV. When we used the XIS + PIN combined spectra, the  $1kT$  model was acceptable as well, with a null-hypothesis probability of 24.5%. Results of the fitting are presented in table 6. As shown in figure 6a, however, the model slightly (by 20%) under-predicted the data in the PIN band. The residual resides right on the 90% upper-limit of the CXB and NXB systematic errors.

The 17' offset data are also consistent with the  $2kT$  picture of the center pointing. In fact, when we applied the  $2kT$  best-fit model of the center pointing to the XIS-PIN spectra, a marginally acceptable fit was obtained by shifting its global normalization by only  $-3\%$  (see also figure 6b). The fit gives  $\chi^2/\text{d.o.f.} = 260.8/222$  or a null-hypothesis probability of 3.8%. In this case, the model slightly (by 20%) over-predicts the PIN data. One possibility is that the cluster as a whole can be represented by the  $2kT$  model, if one includes the systematic errors. The result can also be understood if the very hot component resides within the center XIS FOV, and the majority of the 17' offset XIS FOV is covered by a single  $\sim 7.5$  keV thermal component.

In both the XIS and PIN spectra of the NWR pointing, the CXB and NXB systematic errors are not negligible, as shown in figure 6c. Here, we used the southern 1/3 region of the NWR pointing in the XIS analysis (hereafter 1/3 NW-south region) because the systematic errors make spectral analysis difficult in the other regions. We restricted our fitting to the energy band from 0.7–7.5 keV and 0.7–6.0 keV in the XIS-FI and BI spectra, respectively. We first applied the  $1kT$  model to the XIS spectra. The thus-obtained best-fit temperature

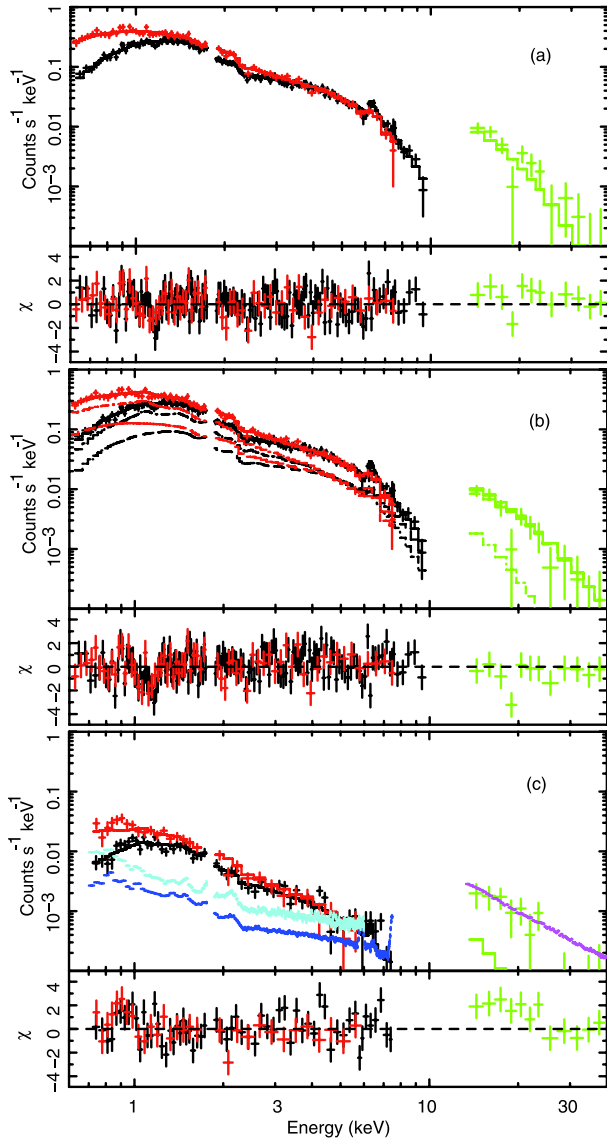


**Fig. 6.** Wide-band spectra of (a) the 17' offset pointing fitted with  $1kT$  model, (b) plotted with a  $2kT$  best-fit model of the central pointing. (c) The NWR spectra with the  $1kT$  best-fit model to the XIS. Cyan, blue, and magenta plots show the typical systematic error of the XIS-FIs, BI, and the PIN spectra. See text for details.

is as low as  $3.6_{-0.7}^{+0.6}$  keV (see table 6), which is significantly cooler than those of the center and 17' offset data. The fit is marginally acceptable with a null-hypothesis probability of 1.5%. Noticeably large residuals appears around 0.9 keV, suggesting an additional  $\sim 1$  keV thermal emission component. The XIS data around the north-west radio relic is further analyzed in sub-subsection 3.4.3.

The NWR PIN signal could be explained by the CXB and NXB systematic errors, since the level is right on their 90% confidence upper-limit (see figure 6c). Another reasonable possibility is the ICM contribution from the cluster central region to the PIN spectra. Based on the arf files derived in subsection 2.4, 37% and 49% of the ICM contribution to the NWR-PIN data originated from within 12.5 and 26' from the

**Table 7.** Spectral parameters of the power-law model.\*

Pointing	$\Gamma$	Flux <sup>†</sup>	$\chi^2/\text{d.o.f.}$
17' offset	$3.4_{-1.0-0.5}^{+1.2+1.0}$	$20_{-4-6}^{+4+6}$	8.4/10
NWR	$3.4_{-1.5-0.9}^{+2.0\text{N/A}\ddagger}$	$5.1_{-1.7-5.1}^{+1.7+6.3}$	7.5/10

\* Fitted to the HXD spectra of the 17' offset and the NWR pointings in the 13–40 keV range.

<sup>†</sup> 10–40 keV flux of the power-law component, in  $10^{-12}$  erg s $^{-1}$  cm $^{-2}$ .

<sup>‡</sup> N/A means the value was not available. In this case, the lack of photon made it impossible to restrict the spectral shape.

cluster X-ray centroid, respectively, which roughly correspond to the area of the center and 17' offset XIS FOVs. As shown later in sub-subsection 3.4.1, the ICM contribution estimated using the XIS can explain all of the PIN signals in the NWR pointing. As a cross check, we also introduce the XMM mosaic data (e.g., Briel et al. 2004) covering the entire PIN FOV later in sub-subsection 3.4.2, and come to the same conclusion.

In table 7, we present the PIN spectral properties separately fitted to the 17' offset and the NWR data. Using the power-law model, the photon index,  $\Gamma$ , becomes as soft as 3.5. Although the error is large, the best-fit value is consistent with those obtained from the center PIN spectra (see table 3), while the flux itself is much brighter there. These results strongly suggest that the same emission dominant in the center-PIN spectra is contaminating both the 17' offset and the NWR PIN data.

### 3.3. Joint Fit to the Wide-Band Spectra of the Three Pointings

The PIN data of the three pointings are all mixed to some extent, mostly contaminated from the emission around the cluster center. In this section, we combine them to obtain the overall cluster properties.

Analyses of the three pointings suggest that all of the data are consistent with the simple two-component picture suggested in the center pointing data, except for the XIS data in the NWR pointing, showing a rather low ICM temperature. Because of its low surface brightness, the thermal contribution from this region is minor in the PIN band. Thus, we conducted a spectral analysis to the data combining in a total of 5 data sets (hereafter all-combined data), i.e., three PIN spectra and the XIS spectra of the center and 17' offset pointings. Following the strategy employed in subsection 3.1, we fixed the relative normalization between the center XIS-FI spectra and all of the PIN spectra, while those between the XISs (offset FI data and all the BI data) were set free to handle small (<5%) residual uncertainties. As noted, the 10% systematic error between the XIS-FI and the PIN data were handled separately.

As was the case with the center pointing, the  $1kT$  model fitting to the all-combined spectra was unsuccessful, giving a  $\chi^2/\text{d.o.f.} = 1430.7/1250$ , or a null-hypothesis probability of  $3 \times 10^{-4}$ . Thus, we applied the  $2kT$  model to the all-combined spectra.

The  $2kT$  fit was almost acceptable, as shown in figure 7 and table 8. The null-hypothesis probability of the fit was 7.6%. Partly because of the slight discrepancy of the spectral shape around 1 keV between the center and the 17' offset pointings, the hotter component temperature was not determined well when the NXB, the CXB, and the arf systematic errors were included

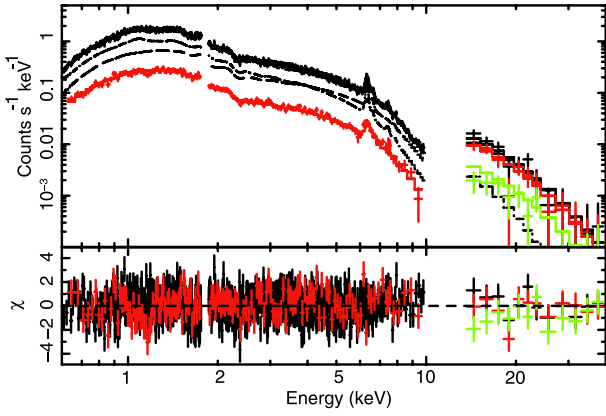


**Fig. 7.** All-combined spectra fitted with the  $2kT$  model. For simplicity, the XIS-BI spectra are not shown, although used in the actual fitting. The XIS and the PIN spectra of the center pointing are shown with black crosses, and those of the 17' offset pointing in red. Green crosses give the PIN spectrum of the NWR pointing. Two components of the model are presented individually as a dashed line only for the center data.

**Table 8.** Best-fit parameters of the  $2kT$  model and  $1kT + PL$  model.\*

	$2kT$	$1kT + PL$
$kT_{lo}$	$4.72^{+0.36+0.01}_{-0.60-2.81}$	$6.40^{+0.15+0.32}_{-0.16-0.43}$
$kT_{hi}$	$14.7^{+3.1+10.4}_{-3.2-7.2}$	—
$Z$	$0.38^{+0.02+0.00}_{-0.02-0.04}$	$0.34^{+0.02+0.02}_{-0.02-0.02}$
$N_{lo}$	$5.6^{+0.8+0.8}_{-1.4-5.0} \times 10^{-2}$	$8.5^{+0.4+0.8}_{-0.3-0.8} \times 10^{-2}$
$N_{hi}$	$4.1^{+1.3+4.8}_{-0.8-1.6} \times 10^{-2}$	—
$\Gamma_{PL}$	—	$1.46^{+0.10+0.01}_{-0.16-0.02}$
$F_{PL}$	—	$25.1^{+5.3+22.5}_{-4.8-21.7}$
$\chi^2/d.o.f.$	1320.4/1248	1364.0/1248

\* Fitted to the all-combined spectra. Columns are similar to those presented in table 4.

in the fit. However, the best-fit value of the hotter component temperature,  $kT_{hi}$ , is still 14.7 keV, which is consistent with the results from the center pointing data (see sub-subsection 3.1.3). The  $3kT$  model gives an acceptable fit, as well.

The  $1kT + PL$  model fitting to the all-combined spectra gave results similar to those of the center pointing (table 8). The fit, itself, was marginally acceptable with a null-hypothesis probability of 1.2%, significantly worse than that of the  $2kT$  model fitting. Although the poor fit could be due to an overly simplified model, the fact that the HXD spectra have a shape as soft as  $\Gamma = 3.5$  strongly indicates emission of thermal origin. Thus, we here conclude that the all-combined fitting also prefers the  $2kT$  (or  $3kT$ ) picture. Another picture that the very hot component resides only around the cluster center may apply as well, considering the systematic errors. In any case, the NWR-PIN data are well explained by the contribution from the cluster central portions, suggesting there is no strong signal of the IC emission in the data.

**Table 9.** Event counts in the 13–40 keV NWR-PIN data.\*

Components	Counts $s^{-1}$
Signal	$(14.1 \pm 4.9) \times 10^{-3}$
4.5% of NXB <sup>†</sup>	$\pm 15.0 \times 10^{-3}$
18% of CXB <sup>‡</sup>	$\pm 4.8 \times 10^{-3}$
ICM <sub>2kT</sub> <sup>§</sup>	$(28.4 \pm 3.0 \pm 2.8) \times 10^{-3}$
ICM <sub>1kT</sub> <sup>§</sup>	$(16.0 \pm 2.0 \pm 1.6) \times 10^{-3}$
ICM <sub>XMM</sub> <sup>§</sup>	$(14.7 \pm 1.5 \pm 1.5) \times 10^{-3}$
Signal <sub>2kT</sub> <sup>  </sup>	$(-14.3 \pm 4.9 \pm 16.3) \times 10^{-3}$
Signal <sub>1kT</sub> <sup>  </sup>	$(-1.9 \pm 4.9 \pm 16.0) \times 10^{-3}$
Signal <sub>XMM</sub> <sup>  </sup>	$(-0.6 \pm 4.9 \pm 15.9) \times 10^{-3}$
$F_{2kT PL}$ <sup>#</sup>	$-5.1 \pm 1.8 \pm 5.8$
$F_{1kT PL}$ <sup>#</sup>	$-0.7 \pm 1.8 \pm 5.7$
$F_{XMM PL}$ <sup>#</sup>	$-0.2 \pm 1.8 \pm 5.7$

\* Compared to various error components.

<sup>†</sup> Estimated NXB systematic error at the 90% confidence.

<sup>‡</sup> Estimated CXB fluctuations at the 90% confidence.

<sup>§</sup> ICM emission component estimated using the  $2kT$  model fitted to the center XIS-PIN combined data, the  $1kT$  model fitted to the 17' offset XIS data, and to the XMM weighted data. Values are shown with 90% fitting error including the NXB+CXB systematic effect in quadrature sum and 10% arf calibration systematic error.

<sup>||</sup> Non-thermal signals in counts  $s^{-1}$  with 90% statistical and systematic errors. The latter value is the quadrature sum of those associated with NXB, CXB, and ICM.

<sup>#</sup> The 10–40 keV band flux in  $10^{-12} \text{ erg s}^{-1} \text{ cm}^{-2}$  derived from the “Signal” column, converted to a  $\Gamma = 2.1$  power law emission.

### 3.4. Search for the IC Signal from the North-West Radio Relic

The north-west radio relic region is mostly covered by the deep (81 ks in the XIS and 48 ks in the HXD) NWR pointing. Although there is no strong evidence for the IC emission in the analysis so far, there should be some X-ray and hard X-ray emission from the relic. In this section, we focused mainly on this region to detect or determine the upper-limit on the IC emission.

#### 3.4.1. The HXD upper limit combined with the XIS results

We evaluated the flux of the possible non-thermal hard X-ray emission using the 13–40 keV PIN signal of the NWR pointing. In table 9, the signal rates are summarized along with their errors. To estimate the ICM components, we used both the  $2kT$  model fitted to the center XIS-PIN combined spectra and the  $1kT$  model fitted to the 17' offset XIS-only spectra. The 17' offset PIN data were not used, because it may contain some signal from the north-west radio relic.

Using the center- $2kT$  model, we converted the residual signal in the NWR-PIN data by assuming a  $\Gamma = 2.1$  fixed power-law emission located at the FOV center. The result is  $(-5.1 \pm 1.8 \pm 5.8) \times 10^{-12} \text{ erg s}^{-1} \text{ cm}^{-2}$ , i.e.,  $< 1.0 \times 10^{-12} \text{ erg s}^{-1} \text{ cm}^{-2}$  in the 10–40 keV band. Here again, the CXB and the NXB systematic errors and the 10% systematic error in the arf files are taken into account. Note that the arf files were used to estimate the ICM contribution, but not in the hard excess flux evaluation. Using the  $1kT$  model fitted to the 17' offset XIS spectra, the power-law flux was estimated to be  $(-0.7 \pm 1.8 \pm 5.7) \times 10^{-12} \text{ erg s}^{-1} \text{ cm}^{-2}$ , i.e.,  $< 5.3 \times 10^{-12} \text{ erg s}^{-1} \text{ cm}^{-2}$  in the 10–40 keV band. Since the

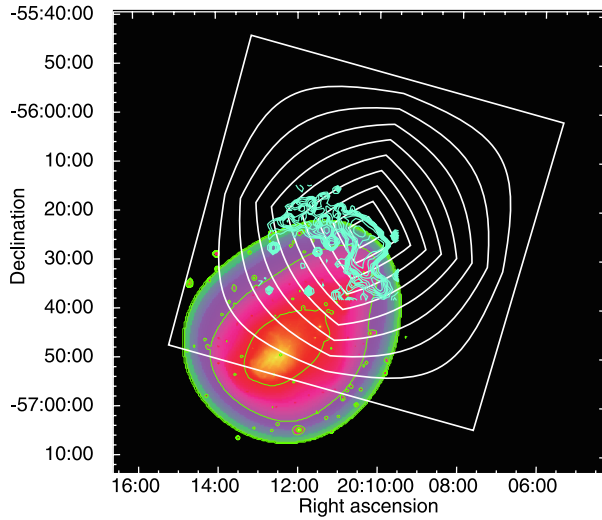


**Fig. 8.** Wavelet smoothed XMM mosaic image of Abell 3667 with a logarithmic color scale (Briel et al. 2004). The white square is the total FOV of the PIN for the NWR observation. The interior white regions are curves of constant PIN effective area, ranging from 10% to 90% of the effective area for a central point source. The cyan contours are from the SUMSS 842 MHz radio image of the NW radio relic. See text for detail.

contribution from the central portion and  $17'$  offset region are both significant, actual upper-limit on the power-law emission will be somewhere between these two values. Here, we recognize the latter results,  $< 5.3 \times 10^{-12} \text{ erg s}^{-1} \text{ cm}^{-2}$ , as the conservative upper-limit flux of the excess hard X-rays from the north-west relic.

### 3.4.2. The HXD upper limit combined with the XMM results

Mapping observations performed by XMM, as described in Briel et al. (2004), provides independent information of the ICM and its temperature distribution. With its larger FOV, the XMM data have a merit of observing almost all of the ICM emission covered by the HXD-PIN FOV, while the XIS has the merit of low background and simpler cross-calibration with the HXD.

The XMM spectra, background and arf files for this analysis are generated using the method described in Wik et al. (2009). In summary, we defined 10 regions with a nearly constant PIN effective area, separated by curves with 0%, 10%, 20%, ..., 90% of the value for the central point source, as shown in figure 8. We then extracted XMM EPIC-pn spectra from these region in the standard manner, using the XMM-mosaic data and adopting the XMMSAS v7.1 calibration. The background spectrum was derived from the datasets compiled by Read and Ponman (2003), and we also apply consistent flare cleaning criteria to both the data and the background. The arf files used for the XMM data included the corrections for exposure and vignetting for the XMM EPIC-pn.

By adding the 10 signal spectra multiplied by the PIN vignetting function, and correcting the XMM-XIS cross normalization of 15%, we obtained the XMM spectrum that would be observed with XMM, but only if it had the spatial response as the Suzaku PIN detector. The normalization of the spectrum is based on the response of the PIN to a point

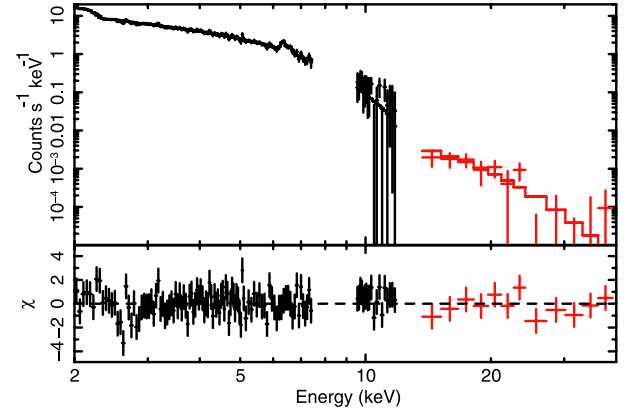


**Fig. 9.** NWR-PIN spectra combined with the XMM spectra. The best-fit  $1kT$  model is shown.

**Table 10.** Best-fit parameters of the  $1kT$  model fitted to the XMM-pn spectra.\*

$kT^\dagger$	Abundance $^\ddagger$	$\chi^2/\text{d.o.f.}$
$7.93^{+0.43}_{-0.42}$	$0.22^{+0.04}_{-0.04}$	116.6/123

\* Weighted with the HXD-PIN vignetting function of the NWR pointing.

$^\dagger$  Temperature of the *apec* model.

$^\ddagger$  Metal abundance of the *apec* model.

source at the center of the PIN field of view; thus, the fluxes are correct if the PIN spectra are fit using the arf appropriate for a central point source. To avoid the contribution of the soft emission components to the results, we performed the spectral fitting above 2 keV, and also masked the energy-region in which the background lines (mostly from Ni) are prominent.

In figure 9, we present the XMM-pn spectra fitted with the  $1kT$  model. The parameters are summarized in table 10. The NWR-PIN spectra are remarkably consistent with the XMM-best-fit model superposed, as also shown in the figure. Thus, using the XMM, we independently obtained a result that no additional hard X-ray component is required in the NWR-PIN data. As shown in table 9, the power-law flux is estimated to be  $(-0.2 \pm 1.8 \pm 5.7) \times 10^{-12} \text{ erg s}^{-1} \text{ cm}^{-2}$ , i.e.,  $< 5.8 \times 10^{-12} \text{ erg s}^{-1} \text{ cm}^{-2}$  in the 10–40 keV band.

### 3.4.3. The XIS Image and Spectral Analysis

Most of the north-west radio relic is covered by the XIS FOVs of the  $17'$  offset and the NWR pointings. Since the background of the XIS is low and stable, the data contains good information on the IC emission from the relic, itself. We then analyzed the XIS spectra obtained from the region as shown in figure 10, which covers 90% of the 847 MHz radio flux (hereafter the north-west relic region). We also examined the projected brightness profile in three energy bands, i.e., 1–2 keV, 2–4 keV, and 4–8 keV, to search for any signal of IC emission.

In the north-west relic region and areas further north, the diffuse X-ray emission is weak and dimmer point sources can be easily identified. As shown in figure 10, we identified two sources with fluxes of  $1.5\text{--}3.5 \times 10^{-14} \text{ erg s}^{-1} \text{ cm}^{-2}$  in the 2–10 keV band, and masked out  $2'$  around them. When we

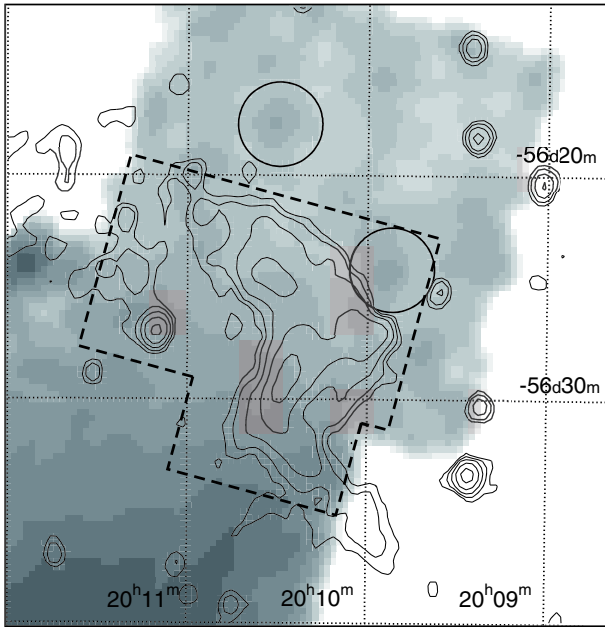


**Fig. 10.** XIS 1–4 keV mosaic image (gray scale) with 843 MHz image overlaid (contours). Regions  $2'$  around the two point sources are shown as solid circles. The north-west relic region, used in the spectral analysis, is shown with thick dashed line.

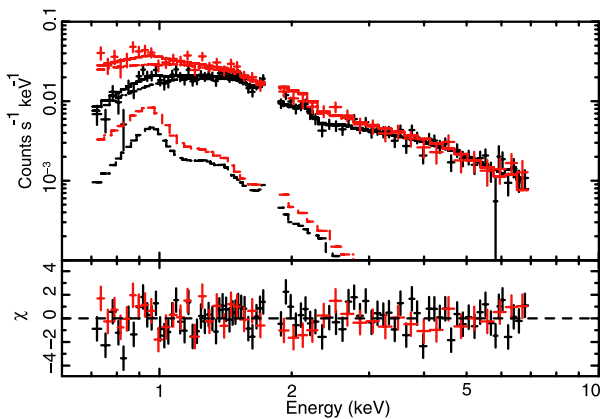


**Fig. 11.** XIS spectra of the north-west relic region fitted with  $2kT$  thermal model. Note the cool component at  $\sim 0.9$  keV.

performed the same operation to the Lockman Hole observation, we found two sources as well. There, the overall CXB level decreased by  $\sim 10\%$  after masking these sources. This shift was fed back into the CXB estimation of the NWR analysis described here. Since the upper cutoff flux changed to  $S_c \sim 2 \times 10^{-14} \text{ erg s}^{-1} \text{ cm}^{-2}$  from  $\sim 1 \times 10^{-13} \text{ erg s}^{-1} \text{ cm}^{-2}$ , the CXB fluctuation level was reduced to 15.9% from the original 21% (see also appendix 1).

In figure 11, the XIS-FI and BI spectra of the north-west relic region data obtained after masking the sources are shown. Both the NWR and  $17'$  offset data were added. To estimate the flux associated with the relic, we calculated the detector response to a widely distributed flat emission accumulated within the north-west relic region, and then scaled it to the

**Table 11.** Power-law model fitted to the XIS spectra of the north-west relic region.

$\Gamma$	Flux*	$\chi^2/\text{d.o.f.}$
$1.8^{+0.1+0.1}_{-0.1-0.1}$	$0.62^{+0.12+0.20}_{-0.10-0.19}$	65.1/66

\* 10–40 keV flux of the power-law component, in  $10^{-12} \text{ erg s}^{-1} \text{ cm}^{-2}$ .

sky coverage ( $\Omega_e = 0.04 \text{ deg}^2$ ) of the region. When fitted with a  $1kT$  model, the fit was marginally acceptable, giving  $\chi^2/\text{d.o.f.} = 158.1/127$  or 3.2% in null hypothesis probability. The temperature was  $5.8 \pm 0.7 \text{ keV}$ , between the two values obtained in the XIS data of the two pointings (see subsection 3.2). To handle the significant hump at around 0.9 keV, we added another thermal component (the  $2kT$  model). We then obtained an almost acceptable fit with  $\chi^2/\text{d.o.f.} = 145.9/125$  or 9.7% in null hypothesis probability. The hot component temperature was derived as  $kT_{\text{hi}} = 7.0^{+2.0}_{-1.6} \text{ keV}$ , and that of the cool one as  $kT_{\text{lo}} = 1.03^{+0.24}_{-0.92} \text{ keV}$ , while the common abundance was  $0.17^{+0.14}_{-0.12}$  solar. The significance of the Fe-K lines is weak, which is not surprising considering the low surface brightness. Since the flux of the cool component at  $\sim 0.9 \text{ keV}$  is similar to that of the CXB model, the emission could be either a slight hump in the “foreground Galactic component” or some cool component really associated with the cluster periphery.

Since the region coincides in position with the diffuse radio emission, the detected X-rays might be of non-thermal origin. As an extreme case, we fit the spectra with a power-law model. Because of the 0.9 keV hump, which indicates a contribution from the  $kT \sim 1 \text{ keV}$  thermal component, we utilized the energy band above 1.5 keV in this fitting. We also limited it to below 6.0 keV, since the NXB systematic error dominates above this energy. The results are listed in table 11. The power-law fit was acceptable with a null-hypothesis probability of 51%. Taking into account the large systematic errors associated with the NXB and CXB (see figure 6c), we cannot distinguish whether the emission is thermal or non-thermal from only spectroscopy.

In figure 12, we present the projected X-ray count-rate map in the energy bands of 1–2 keV, 2–4 keV, and 4–8 keV derived from all three XIS-FI detectors. Here, the BI chip is not utilized because of its higher background. Regions around the two point source in the NWR data are excluded in the plot. Overlaid is a profile of the SUMSS 843 MHz radio image, which clearly shows the relic, located  $\sim 30'$  (2 Mpc) away from the X-ray centroid. From the 1–2 keV and 2–4 keV profiles, it is clear that the cluster emission was detected out to a region  $40'$  from the cluster X-ray centroid, which corresponds to 2.6 Mpc in projected distance. On the other hand, there is apparently no excess signal associated with the radio relic, smoothly connecting the inner ICM X-rays to the CXB component at the outermost region. Thus, a significant fraction of the X-rays in the NWR region was naturally assumed to be of thermal origin.

Using this plot, we roughly evaluated the upper-limit of the projected non-thermal count rates associated with the relic. Here, we assumed that the IC emission has the same morphology as that of the radio emission, and the 2–8 keV X-ray counts within region B in figure 12 are the upper-limit

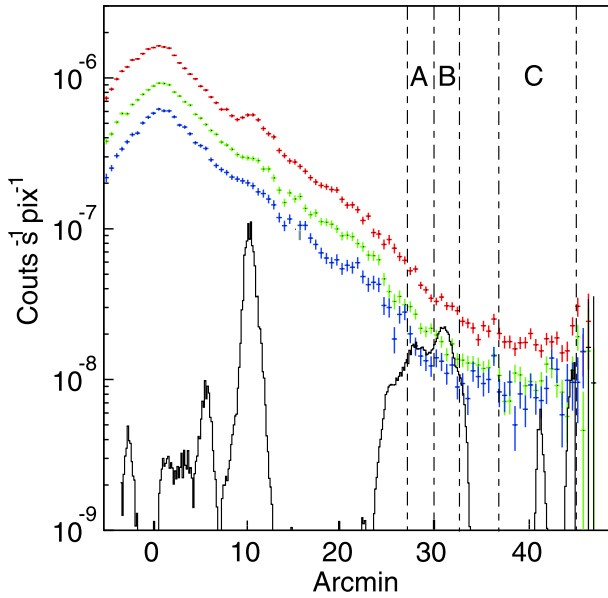


**Fig. 12.** Projected X-ray image in the energy band of 1–2 keV, 2–4 keV, and 4–8 keV in red, green, and blue crosses, respectively. The width of the projection region is 12' along the merger axis, as shown in figure 1. Black histogram stands for SUMSS 843 MHz radio image obtained via Skyview service by NASA, projected in the same manner, but with arbitrary normalization. Regions A, B, and C are those used for IC upper-limit analysis. See text for detail.

to the IC emission. The CXB was estimated from region C, and its fluctuation was calculated to be 22% in both regions A and B. Taking the statistical error and the CXB fluctuation into account, the relative count-rate of region B to that of region A was derived as  $0.48^{+0.22}_{-0.17}$ , while that of the radio flux was 1.17. Thus, we concluded that  $40^{+16}_{-16}\%$ , i.e., larger than 24%, of the emission in region A+B was of thermal origin. Since region A+B coincided with the north-west relic region, we combined this result with the power-law fitting results (table 11). In addition, because the radio emission within the spectral fitting region only covers 90% of the total relic flux in the SUMSS image, we multiplied the XIS flux by a factor of 1.1 to account for any missing nonthermal flux. Finally, we obtained the 10–40 keV upper limit IC flux for the north-west radio relic as a whole as  $7.3 \times 10^{-13} \text{ erg s}^{-1} \text{ cm}^{-2}$ , while allowing  $\Gamma$  to vary, at the 90% confidence level. With this flux, the photon index was required to be  $\Gamma = 1.6$ . If we fix it to  $\Gamma = 2.1$ , the 10–40 keV upper limit flux becomes  $3.9 \times 10^{-13} \text{ erg s}^{-1} \text{ cm}^{-2}$ .

## 4. Discussion

### 4.1. Short Summary of the Analysis Results

We analyzed the Suzaku mapping observation data of a merging cluster, Abell 3667. The XIS detected emission from the cluster out to  $\sim 40'$  or 2.6 Mpc from the cluster X-ray centroid. The PIN spectra of the three pointings commonly prefer soft-shaped spectra, suggesting that the thermal contribution from the cluster ICM is the major origin of these signals. From the XIS + PIN combined analysis of the center pointing, a multi-phase picture, such as the  $2kT$  model, the  $1kT$  + PL

model, or the  $3kT$  model, is suggested. In the former case,  $kT_{\text{hi}}$  was derived to exceed 13.2 keV, with the best-fit value around 20 keV, while  $kT_{\text{lo}}$  was around 4.7 keV. Using the  $3kT$  model with one of the temperatures fixed at 7.5 keV, the fit was also acceptable, while a component with  $kT_{\text{hi}} \sim 20$  keV was still required. This result suggests the existence of a very hot ( $kT \sim 20$  keV) component around the cluster center.

The XIS spectra of the 17' offset pointing can be fitted using the  $1kT$  model with  $kT \sim 7.5$  keV, while that of the southern one third of the NWR pointing (the 1/3 NW-south region) requires a cooler value, around 4 keV. The PIN signal in the NWR pointing, as well as the 17' offset pointing, can be explained by the ICM contribution with either the  $2kT$  picture, suggested by the center pointing, or the  $1kT$  picture fitted to the 17' offset XIS data. The shape of the PIN spectra of the center and 17' offset pointings are too soft to account for the  $\Gamma = 2.1$  IC emission suggested from the radio observation. Thus, the wide-band Suzaku X-ray spectra do not show any signature of the IC emission associated with the strong (3.7 Jy at 1.4 GHz) radio synchrotron emission.

Using the HXD, the overall upper-limit 10–40 keV flux on the non-thermal emission within a  $34' \times 34'$  FOV around the north-west radio relic was derived to be  $5.3 \times 10^{-12} \text{ erg s}^{-1} \text{ cm}^{-2}$  with the  $1kT$  ICM modeling. The ICM modeling using the XMM-pn spectra gave a similar upper limit. Using the XIS, the upper-limit on the IC emission from the radio relic, itself, was derived to be  $3.9 \times 10^{-13} \text{ erg s}^{-1} \text{ cm}^{-2}$ , when converted into the 10–40 keV band and assuming  $\Gamma = 2.1$ . If we allowed the index to be free, i.e., assume that there is a spectral break somewhere above 10 keV, the upper-limit value became  $7.3 \times 10^{-13} \text{ erg s}^{-1} \text{ cm}^{-2}$ .

### 4.2. The Magnetic Field in the North-West Radio Relic

By combining the radio and X-ray observations, here we estimate the magnetic field strength in the north-west radio relic. From the radio observation, the relic has a flux of 3.7 Jy at 1.4 GHz (Johnston-Hollit et al. 2008). Its radio fluxes at 85 MHz, 843 MHz, 1.4 GHz, and 2.3 GHz are reported to roughly follow the power law with  $\Gamma = 2.1$  (Röttgering et al. 1997). With a magnetic field of  $1 \mu\text{G}$ , the 85 MHz radio emission requires electrons with a Lorentz factor,  $\gamma$ , of  $\sim 5 \times 10^3$ , which in turn emits IC photons at around 20 keV. In the case of 1.4 GHz radio emission, they are  $\gamma \sim 2 \times 10^4$  and 350 keV, respectively. Thus, we will assume that the photon index is similar to  $\Gamma = 2.1$  above 20 keV, when the magnetic field is stronger than  $1 \mu\text{G}$ .

The radio flux at the 80–320 MHz band, which corresponds to the  $\sim 20$  keV IC emission with  $B = 1 \mu\text{G}$ , was derived as  $F_{80-320 \text{ MHz}}^{\text{Sync}} = 1.8 \times 10^{-13} \text{ erg s}^{-1} \text{ cm}^{-2}$ , assuming a  $\Gamma = 2.1$  power-law emission and a flux of 3.7 Jy at 1.4 GHz. The XIS upper-limit right on the north-west radio relic region was derived as  $F_{10-40 \text{ keV}}^{\text{IC}} < 3.9 \times 10^{-13} \text{ erg s}^{-1} \text{ cm}^{-2}$ , again assuming a simple  $\Gamma = 2.1$  power law. By dividing these two values, we obtain

$$\frac{F_{80-320 \text{ MHz}}^{\text{Sync}}}{F_{10-40 \text{ keV}}^{\text{IC}}} = \frac{U_B}{U_{\text{CMB}}} = \left( \frac{B}{B_{\text{eq}}^{\text{CMB}}} \right)^2 > \frac{1.8 \times 10^{-13}}{3.9 \times 10^{-13}}. \quad (1)$$

Here,  $B_{\text{eq}}^{\text{CMB}} = 3.2 \mu\text{G}$  is the equivalent magnetic field of the

energy density of the CMB. Thus, the magnetic field in the north-west radio relic is inferred to be  $B > 2.2 \mu\text{G}$ .

Since the radio emission is detected only down to 85 MHz, the IC spectra below  $\sim 20$  keV might have a break. For electrons with  $\gamma = 5 \times 10^3$  within a thermal gas density of  $\sim 1.3 \times 10^{-4} \text{ cm}^{-3}$  (derived from the XIS results), the dominant cooling processes are the IC and the synchrotron emissions. These give a cooling time of  $\sim 4 \times 10^8$  yr. If the duration of electron injection is shorter than this time-scale, the electron distribution below this energy is not affected by the cooling, and the resultant IC (and synchrotron) photon index can be harder, typically  $1.5 < \Gamma < 2.1$ . From the  $\Gamma$  free power-law fitting to the XIS spectra obtained from the north-west relic region, we know that the upper-limit IC flux in the 10–40 keV band is  $7.3 \times 10^{-13} \text{ erg s}^{-1} \text{ cm}^{-2}$ . In this model, the photon index is 1.6 around 4 keV, and breaks to 2.1 above  $\sim 20$  keV. In this case, the magnetic field strength is inferred to be  $B > 1.6 \mu\text{G}$ . These results are consistent with the radio rotation measure observations of this relic, suggesting 3–5  $\mu\text{G}$  (Johnston-Hollitt 2004).

Based on the observable parameters, we calculate the energy density of individual components in the north-west radio relic. The thermal particle density and temperature give an energy density,  $U_{\text{th}}$ , of  $1.0 \text{ eV cm}^{-3}$ . Here, we simply assume that all X-rays in the north-west relic are of thermal origin. With a magnetic field strength of  $> 2.2 \mu\text{G}$  and  $> 1.6 \mu\text{G}$ , the energy density,  $U_B$ , is derived as  $> 0.12 \text{ eV cm}^{-3}$  or  $> 0.07 \text{ eV cm}^{-3}$ , respectively. Here, on the contrary, we assume that most of the X-rays are of IC origin to give an upper limit on  $U_e$ . If a power-law distribution of relativistic electrons is assumed within  $5 \times 10^2 < \gamma < 4 \times 10^4$ , the energy density of electrons,  $U_e$ , is  $< 0.15 \text{ eV cm}^{-3}$ . Here, the minimum  $\gamma$  is assumed to be the critical Lorentz factor below where ionization losses dominate (Sarazin 1999). Although  $U_e$  strongly depends on the unknown electron distribution below  $\gamma \sim 5 \times 10^3$ , the calculated upper-limit value is not so far from the equi-partition condition.

The ratio between the non-thermal ( $U_B$  and  $U_e$ ) and thermal ( $U_{\text{th}}$ ) energy density is inferred to be as large as 20%. Although  $U_e$  has a large uncertainty, the lower limit on  $U_B$  is much more robust. In addition,  $U_B/U_{\text{th}} > 0.07$  is a strong limit. If we assume, for example, that about half of the X-rays in the north-west relic are of thermal origin and the latter half is of IC origin,  $U_{\text{th}}$  is decreased by a factor of  $\sqrt{2}$ , and the lower limit on the  $U_B$  is doubled. In this case, the ratio becomes as high as 19%, excluding the  $U_e$  contribution. Our results are generally consistent with those by Röttgering et al. (1997), though they do not discuss in detail the magnetic field.

This demonstrates that magnetic fields stronger than  $1 \mu\text{G}$  exist on scales as large as the cluster virial radius, and exert non-negligible pressure compared to the thermal one, at least around the region of the north-west relic. Recent observations of radio relics around other clusters have also revealed similarly strong magnetic fields of  $> 0.8 \mu\text{G}$  (e.g., Henriksen & Mushotzky 2001; Feretti & Neumann 2006; Hubert et al. 2008). That of the Abell 3667 north-west relic is the strongest yet observed.

It is important to note that the large magnetic field we found applies only to the interior of the radio relic. Thus, it is possible that most clusters do not have such large fields at such outer

radii. The relic is the brightest diffuse cluster radio source known, and its interior may not be typical of the diffuse intra-cluster medium outside the relic, or in other clusters. It may be that the magnetic field and seed relativistic particles were injected into this region by an AGN in the past (e.g., Enßlin & Gopal-Krishna 2001). If the relativistic electrons were accelerated by a merger shock, the same shock may have amplified the magnetic field, perhaps by some mechanism like the Weibel instability (e.g., Okabe & Hattori 2003; Fujita et al. 2006; Kato 2007) or the cosmic-ray streaming instability (Lucek & Bell 2000; Bell 2004). Also, Abell 3667 has undergone a very dramatic merger, and may not be typical of more relaxed clusters.

#### 4.3. Comparison of the HXD-PIN Upper-Limit of the IC Emission with Other Results

The HXD-PIN data of the NWR pointing provides an upper-limit on the IC emission as  $5.3 \times 10^{-12} \text{ erg s}^{-1} \text{ cm}^{-2}$ . Since the FOV of the PIN is  $\sim 10$ -times larger than the region used in the XIS analysis, it provides valuable limits on any non-thermal electrons that may be distributed on scales larger than the north-west relic. These electrons, in addition, are not readily observable in the radio band. For example, if the relic is surrounded by a larger region with a lower magnetic field, say  $0.3 \mu\text{G}$ , electrons therein with  $\gamma \sim 5 \times 10^3$  would be unobservable through their synchrotron emission, since its frequency is less than 10 MHz.

Using the Beppo-SAX PDS data with an equivalent exposure (113 ks) to the NWR pointing, Fusco-Femiano et al. (2001) derived an upper-limit hard X-ray flux of  $\sim 6.4 \times 10^{-12} \text{ erg s}^{-1} \text{ cm}^{-2}$  in the 20–80 keV band, assuming a  $\Gamma = 2.1$  power-law emission. Here, they fixed the ICM temperature to 7 keV, and included only the statistical errors. Using the same data with a similar thermal model, Nevalainen et al. (2004) presented a 90% confidence upper limit flux of  $7.1 \times 10^{-12} \text{ erg s}^{-1} \text{ cm}^{-2}$  in the same energy band, assuming a power-law with  $\Gamma = 2.0$ . The main difference in the two results is that the latter author took into account the possible systematics in the PDS background modeling and AGN contribution derived in their own manner.

By comparing the observational results on Crab Nebula, we found that the 20–80 keV flux derived from Beppo-SAX PDS is 21% smaller than those derived from Suzaku. Thus, results from Fusco-Femiano et al. (2001) and Nevalainen et al. (2004) can be converted into Suzaku-equivalent fluxes of 8.1 and  $9.0 \times 10^{-12} \text{ erg s}^{-1} \text{ cm}^{-2}$ , respectively. Therefore, our Suzaku result provides a more stringent upper limit on the flux, compared to these two results. Furthermore, it is focused on a more spatially restricted region around the north-west radio relic, thanks to the narrow FOV of the HXD ( $\phi \sim 34'$  FWHM) compared to that of the PDS ( $\phi \sim 1.3'$  FWHM).

#### 4.4. Possible Very Hot Component in the Merging Cluster

The HXD-PIN results from the cluster center shows a “soft-shaped” hard component with  $\Gamma = 3.6_{-0.9}^{+1.1}$ , which can be best interpreted as a very hot component with a temperature of  $19.2_{-6.0}^{+6.6} \text{ keV}$ , in addition to the  $\sim 4.7 \text{ keV}$  component in the  $2kT$  picture combined with the XIS spectra. Using the  $3kT$  model, the temperature of the very hot component is required

to be higher than 20 keV. Since the spectra can be marginally fitted with a  $\Gamma \sim 1.4$  power-law component as well, the emission could be of non-thermal origin, or contamination from a yet unknown Compton-thick AGN. However, our contaminating point-source survey (appendix 3) and the softness of the spectral shape, itself, suggests the thermal interpretation. Since the excess signal to the  $1kT$  component is significant in the center pointing, the very hot component can be significant around the cluster center. Detailed modeling of the ICM using all of the available data, including our new XMM data to be obtained soon, will help to clarify the actual value.

From the ASCA observations, this cluster is known to host significant temperature inhomogeneity, showing regions with a temperature as high as 10 keV, together with the 4–6 keV dominant emission (Markevitch et al. 1999). Later Briel et al. (2004) also showed the complex multi temperature nature of the ICM using the XMM data. The temperature ranges from 4 keV to 8 keV, and several hot regions are visible around the cluster center. Since these analyses are based on the projected X-ray color maps, the temperature of the actual hottest component can be higher, considering the convolution along the line-of-sight. The Beppo-SAX PDS spectrum is consistent with the center- $2kT$  model taking into account all the systematic errors. Thus, our results on the “soft-shaped” hard component is basically consistent with existing data.

Such a very hot component, with a temperature as high as 20 keV is suggested by many hydrodynamical simulations of merging clusters right after the time of impact (e.g., Takizawa 2000; Ricker & Sarazin 2001). Since the Abell 3667 cluster is considered to be at this stage, the very hot component will be the hottest heated ICM emission. We note that a similar very hot component is suggested in the cluster RX J1347.5–1145 (Ota et al. 2008) using the Suzaku wide-band data combined with Chandra spectra. Its high temperature and relatively large luminosity means that the very hot component cannot be in pressure balance with the cooler one; otherwise, it will dominate the volume in the cluster. Thus, the emission should be temporary originating from the shock and/or the compression heating, and is expected to disappear soon by adiabatic expansion. To investigate the location of the emission, we will need much wider energy band coverage in the imaging detector, specifically, arcminute-scale imaging spectroscopy up to  $\sim 40$  keV.

## 5. Conclusion

From Suzaku mapping observations of Abell 3667, upper-limits on the non-thermal (hard) X-ray emission were obtained. On the north-west radio relic, itself, the XIS limit of  $7.3 \times 10^{-13} \text{ erg s}^{-1} \text{ cm}^{-2}$  extrapolated to the 10–40 keV band provides a lower-limit magnetic field of  $> 1.6 \mu\text{G}$ . The non-thermal energy density there is estimated to be higher than 7%, and likely near 20%.

By combining the XIS and the XMM mapping data to the HXD-PIN spectra, the upper limit on the 10–40 keV excess hard emission was derived as  $1.0\text{--}5.3 \times 10^{-12} \text{ erg s}^{-1} \text{ cm}^{-2}$ , depending on the modeling of the ICM. Since the north-west relic has a magnetic field of  $> 1 \mu\text{G}$ , and hence must be almost an order of magnitude darker than this hard X-ray limit, the

relativistic electrons must be distributed in regions other than the relic with low magnetic field (of  $B < 0.3 \mu\text{G}$ ) if IC hard X-ray emission near the flux limit exists.

The PIN data from the pointing on the cluster center shows hard X-rays in excess to the averaged ICM emission, which is thought to have a temperature of around 7 keV. Although other interpretations cannot be rejected, its soft spectral shape indicates the emission to be possibly from a very hot thermal component with a temperature of  $\sim 20$  keV, generated temporary in the cluster merger phase.

In the near future, X-ray observatories with hard X-ray imaging optics operating up to 40 keV will be launched, such as the ASTRO-H (former NeXT; e.g., Takahashi et al. 2006), NuSTAR and Simbol-X (e.g., Ferrando et al. 2006). These detectors will drastically improve the sensitivity to both point sources and relatively clumpy extended hard X-rays, such as the local non-thermal emission associated with the radio halos/relics and the very hot component. In addition, the Soft Gamma-ray Detector onboard ASTRO-H, (a collimated instrument) features the highest sensitivity at around 100 keV using the novel narrow-field-of-view Compton camera concept. It will open a new window to the widely distributed non-thermal emission, which is difficult to separate from the ICM thermal emission below  $\sim 50$  keV.

K.N. and K.M. are supported in part by a Grant-in-Aid from the Ministry of Education, Science, Sports, and Culture (18104004), and M.T. (16740105, 19740096) and S.I. (19047004, 19540283), as well. C.L.S. and D.R.W. were supported by NASA Suzaku grants NNX06AI44G and NNX06AI37G and XMM-Newton grant NNX06AE76G. D.R.W. was also supported by a DuPont Fellowship and a Virginia Space Grant Consortium Fellowship. A.F. was partially supported by NASA grant NNG05GM50G to UMBC. Basic research in radio astronomy of T.C. at the NRL is supported by 6.1 Base funding.

## Appendix 1. The CXB Estimation for the XIS

The Lockman Hole observation (Suzaku observation ID, 101002010) was used as the CXB template. The NXB subtracted data from the Lockman Hole were fitted with a model composed of a power law with a fixed  $\Gamma$  of 1.4, and thermal components (so called Galactic components) with one of the temperatures fixed at 0.08 keV and another fitted to give  $\sim 0.3$  keV. The 2–10 keV flux of the power-law component was derived as  $5.7 \pm 0.1 \times 10^{-8} \text{ erg s}^{-1} \text{ cm}^{-2} \text{ str}^{-1}$ , which is consistent within  $1\sigma$  from the best-fit value derived using ASCA (Kushino et al. 2002).

We also analyzed the XIS data of the outer boundary for Abell 3667, using the northern 1/3 region of the NWR pointing (hereafter the 1/3 NW-north region). It gave a  $\sim 16\%$  higher normalization for the power-law component, which is consistent with the expected fluctuation of CXB, discussed later in this section. The “Galactic component” parameters are similar, but the flux is brighter by a factor of 2–5, which is also consistent with its sky fluctuations. Because the 1/3 NW-north region could be contaminated by the outskirts of the cluster ICM emission, we modeled the CXB with the power-law component

fixed at the value obtained from the Lockman Hole observation, while the ‘‘Galactic component’’ was fixed at that of the 1/3 NW-north region.

The CXB fluctuations can be modeled as  $\sigma_{\text{CXB}}/I_{\text{CXB}} \propto \Omega_e^{-0.5} S_c^{0.25}$ . Here,  $\Omega_e$  is the effective solid angle and  $S_c$  is the upper cutoff flux. From the HEAO-1 A2 results, Shafer (1983) derived  $\sigma_{\text{CXB}}/I_{\text{CXB}} = 2.8\%$ , with  $\Omega_e = 15.8 \text{ deg}^2$  and  $S_c = 8 \times 10^{-11} \text{ erg s}^{-1} \text{ cm}^{-2}$ . By scaling this result with the XIS parameters, i.e.,  $\Omega_e = 0.09 \text{ deg}^2$  and  $S_c \sim 1 \times 10^{-13} \text{ erg s}^{-1} \text{ cm}^{-2}$  in the cluster vicinity, we obtained the CXB fluctuation over the XIS full FOV as 11% (90% confidence level). For the NWR 1/3 NW-north region, the value is then 19%. For the north-west relic region with  $\Omega_e = 0.04 \text{ deg}^2$  and  $S_c \sim 2 \times 10^{-14} \text{ erg s}^{-1} \text{ cm}^{-2}$ , it becomes 15.9%. Note that this scaling relation is consistent with the ASCA and Ginga CXB analysis (Ishisaki 1997).

## Appendix 2. The CXB Estimation for the HXD

The CXB flux in the PIN was modeled as a cutoff power-law, described as  $N(E) = n \times (E)^{-\Gamma} \times \exp(-E/E_{\text{fold}})$  in photons  $\text{cm}^{-2} \text{ s}^{-1} \text{ keV}^{-1} \text{ FOV}^{-1}$ . Here,  $E_{\text{fold}}$  is the folding energy, and  $n$  is the normalization. If energies below  $\sim 80 \text{ keV}$ , the HXD energy response for a diffuse source is the same as that for a point source, except for its normalization. Thus, we simply scaled our CXB model to the solid angle of the HXD,  $\Omega_e^{\text{HXD}} = 0.32 \text{ deg}^2$  and utilized the HXD nominal response. We first used the parameters based on the HEAO-1 results (Boldt 1987), which gave  $\Gamma = 1.29$ ,  $E_{\text{fold}} = 40.0$ , and  $n = 8.36 \times 10^{-4}$ . We then compared this model to the XIS observation of Lockman Hole, on which our XIS CXB modeling is based on. It was found that the model predicts a flux 8.6% lower in the XIS 3–8 keV band data. Thus, we modified the PIN CXB model normalization to match the difference, as  $n = 8.69 \times 10^{-6}$ . Note that although there is an apparent difference in photon index between the CXB model of the XIS and PIN, the cutoff function in the later makes two models perfectly matched in the energy band at 3–8 keV. Through the same approach was applied to the XIS data, the CXB fluctuation in the HXD FOV is expected to be 18%, with  $\Omega_e^{\text{HXD}} = 0.32 \text{ deg}^2$  and a conservative upper cutoff flux of  $S_c \sim 8 \times 10^{-12} \text{ erg s}^{-1} \text{ cm}^{-2}$  in the 10–40 keV band.

## Appendix 3. Estimation of Point Source Contamination in the FOV of the PIN

Since the PIN has a wider FOV ( $68' \times 68'$  bottom to bottom) than that of the XIS ( $18' \times 18'$ ) and also lacks imaging capability, signal contamination from point sources within the FOV should be carefully estimated. Figure 13 shows a PSPC image

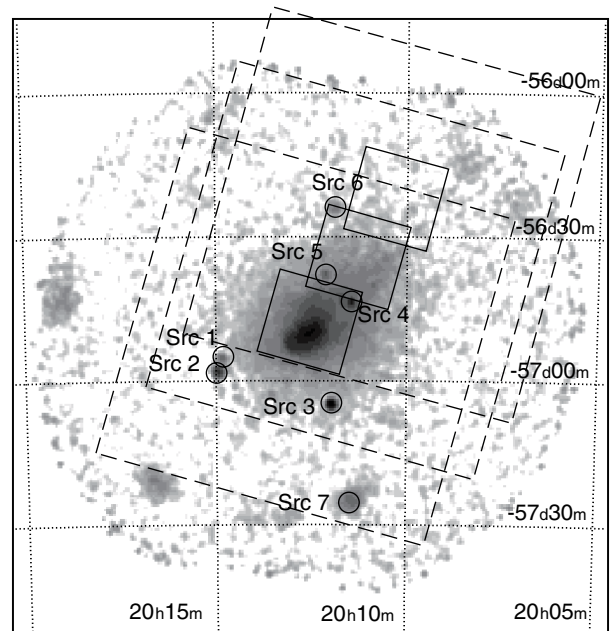


**Fig. 13.** Background subtracted ROSAT PSPC image (50' radius) of Abell 3667. Gray-scale contour is logarithmic scale. The FOVs ( $68' \times 68'$  bottom to bottom) of PIN are shown in dashed thin rectangles, those of the XIS are shown in solid rectangles, and X-ray point sources in the FOVs are shown in circles.

of Abell 3667 with the FOVs of the PIN superposed. The PSPC data were processed by a method described by Snowden et al. (1994). There exists seven X-ray point sources in the PIN FOVs. We identified these sources using the SIMBAD astronomical database.

Source 4 and Source 6 are in the FOV of XIS, and thus their flux was estimated by the XIS data. Although the other sources are outside the FOV of XIS, archival data of ASCA GIS are available for sources 1, 2, 3, and 5. We therefore extracted the GIS spectra of source 1 thorough source 6, and fitted them with a power law modified by galactic absorption. Blank sky observations of the GIS were used for the background of sources 1, 2, and 3, while the neighboring field was used for source 5.

Using the best-fit parameters, we simulated the PIN spectra of the six sources for the three pointings, considering the PIN transmission to each of them on the three pointings. The total contribution of the six point sources, thus estimated is more than an order of magnitude lower than the detected signal, and is hence negligible. Source 7, not included in this estimation, is located at the boundary of the PIN FOV of the center pointing. It is also a weak hard X-ray source, since it is a distant cluster of galaxies.

## References

- Anders, E., & Grevesse, N. 1989, *Geochim. Cosmochim. Acta*, 53, 197  
 Bell, A. R. 2004, *MNRAS*, 353, 550  
 Boldt, E. 1987, *IAU Circ.*, 124, 611  
 Briel, U. G., Finoguenov, A., & Henry, J. P. 2004, *A&A*, 426, 1  
 Carilli, C. L., & Taylor, G. B. 2002, *ARA&A*, 40, 319  
 Clarke, T. E., Kronberg, P. P., & Böhringer, H. 2001, *ApJ*, 547, L111  
 Dickey, J. M., & Lockman, F. J. 1990, *ARA&A*, 28, 215  
 Enßlin, T. A., & Gopal-Krishna, 2001, *A&A*, 366, 26  
 Feretti, L., & Neumann, D. M. 2006, *A&A*, 450, L21

- Ferrando, P., et al. 2006, *Proc. SPIE*, 6266, 11
- Fujita, Y., Kato, T. N., & Okabe, N. 2006, *Phys. Plasmas*, 13, 122901
- Fukazawa, Y., et al. 2009, *PASJ*, 61, S17
- Fukazawa, Y., Makishima, K., & Ohashi, T. 2004, *PASJ*, 56, 965
- Fukazawa, Y., Nakazawa, K., Isobe, N., Makishima, K., Matsushita, K., Ohashi, T., & Kamae, T. 2001, *ApJ*, 546, L87
- Fusco-Femiano, R., Dal Fiume, D., Feretti, L., Giovannini, G., Grandi, P., Matt, G., Molendi, S., & Santangelo, A. 1999, *ApJ*, 513, L21
- Fusco-Femiano, R., Dal Fiume, D., Orlandini, M., Brunetti, G., Feretti, L., & Giovannini, G. 2001, *ApJ*, 552, L97
- Fusco-Femiano, R., Landi, R., & Orlandini, M. 2007, *ApJ*, 654, L9
- Henriksen, M., & Mushotzky, R. 2001, *ApJ*, 553, 84
- Hubert Chen, C. M., Harris, D. E., Harrison, F. A., & Mao, P. H. 2008, *MNRAS*, 383, 1259
- Inoue, S., Aharonian, F. A., & Sugiyama, N. 2005, *ApJ*, 628, L9
- Ishisaki, Y. 1997, Ph.D. thesis, The University of Tokyo
- Johnston-Hollitt, M. 2004, in *Proc. The Riddle of Cooling Flows in Galaxies and Clusters of Galaxies*, ed. T. H. Reiprich, J. C. Kempner, & N. Soker, 51
- Johnston-Hollitt, M., Hunstead, R. W., & Corbett, E. 2008, *A&A*, 479, 1
- Kato, T. N. 2007, *ApJ*, 668, 974
- Kokubun, M., et al. 2007, *PASJ*, 59, S53
- Koyama, K., et al. 2007, *PASJ*, 59, S23
- Kushino, A., Ishisaki, Y., Morita, U., Yamasaki, N. Y., Ishida, M., Ohashi, T., & Ueda, Y. 2002, *PASJ*, 54, 327
- Lucek, S. G., & Bell, A. R. 2000, *MNRAS*, 314, 65
- Markevitch, M., Sarazin, C. L., & Vikhlinin, A. 1999, *ApJ*, 521, 526
- Mazzotta, P., Fusco-Femiano, R., & Vikhlinin, A. 2002, *ApJ*, 569, L31
- Mitsuda, K., et al. 2007, *PASJ*, 59, S1
- Mohr, J. J., Mathiesen, B., & Evrard, A. E. 1999, *ApJ*, 517, 627
- Nakazawa, K., Makishima, K., & Fukazawa, Y. 2007, *PASJ*, 59, 167
- Neumann, D. M., & Arnaud, M. 1999, *A&A*, 348, 711
- Nevalainen, J., Oosterbroek, T., Bonamente, M., & Colafrancesco, S. 2004, *ApJ*, 608, 166
- Okabe, N., & Hattori, M. 2003, *ApJ*, 599, 964
- Ota, N., et al. 2008, *A&A*, 491, 363
- Petrosian, V., Madejski, G., & Luli, K. 2006, *ApJ*, 652, 948
- Read, A. M., & Ponman, T. J. 2003, *A&A*, 409, 395
- Rephaeli, Y., Gruber, D., & Arieli, Y. 2006, *ApJ*, 649, 673
- Ricker, P. M., & Sarazin, C. L. 2001, *ApJ*, 561, 621
- Rossetti, M., & Molendi, S. 2004, *A&A*, 414, L41
- Röttgering, H. J. A., Wieringa, M. H., Hunstead, R. W., & Ekers, R. D., 1997, *MNRAS*, 290, 577
- Sarazin, C. L. 1986, *Rev. Mod. Phys.*, 58, 1
- Sarazin, C. L. 1999, *ApJ*, 520, 529
- Shafer, R. A. 1983, PhD Thesis, University of Maryland
- Snowden, S. L., McCammon, D., Burrows, D. N., & Mendenhall, J. A. 1994, *ApJ*, 424, 714
- Sodre, L. Jr., Capelato, H. V., Steiner, J. E., Proust, D., & Mazure, A. 1992, *MNRAS*, 259, 233
- Struble, M. F., & Rood, H. J. 1999, *ApJS*, 125, 35
- Takahashi, T., et al. 2007, *PASJ*, 59, S35
- Takahashi, T., Mitsuda, K., & Kunieda, H. 2006, *Proc. SPIE*, 6266, 10
- Takizawa, M. 2000, *ApJ*, 532, 183
- Tawa, N., et al. 2008, *PASJ*, 60, S11
- Vikhlinin, A., Markevitch, M., & Murray, S. S. 2001a, *ApJ*, 549, L47
- Vikhlinin, A., Markevitch, M., & Murray, S. S. 2001b, *ApJ*, 551, 160
- Watanabe, M., Yamashita, K., Furuzawa, A., Kunieda, H., Tawara, Y., & Honda, H. 1999, *ApJ*, 527, 80
- Wik, D. R., Sarazin, C. L., Finoguenov, A., Matsushita, K., Nakazawa, K., & Clarke, T. E. 2009, *ApJ*, in press